2012-04-23

Application of Two-Color Pyrometry to Characterize the Two-Dimensional Temperature and Emissivity of Pulverized-Coal Oxy-Flames

Teri Snow Draper
Brigham Young University - Provo

Application of Two-Color Pyrometry to Characterize the Two-Dimensional

Temperature and Emissivity of Pulverized-Coal Oxy-Flames

Teri Snow Draper

A thesis submitted to the faculty of
Brigham Young University
in partial fulfillment of the requirements for the degree of

Master of Science

Dale R. Tree, Chair
Matthew R. Jones
David O. Lignell

Department of Mechanical Engineering

Brigham Young University

June 2012

ABSTRACT

Application of Two-Color Pyrometry to Characterize the Two-Dimensional
Temperature and Emissivity of Pulverized-Coal Oxy-Flames

Teri Snow Draper
Department of Mechanical Engineering, BYU
Master of Science

Oxy-combustion is a developing technology that enables carbon dioxide (CO_2) capture. Flame temperature and emissivity data were taken on a 150 kW_{th}, pulverized-coal, burner flow reactor (BFR) that has been modified to run oxy-combustion with pure CO_2 as simulated recycled flue gas. Data were taken at 78 conditions in which three parameters were varied, namely: the swirl angle of the fuel stream, the location of the oxidizer as it exited the burner, and the flow rate of diluent (pure CO_2) added to the outer, secondary stream. At each condition, digital color images were obtained using a calibrated RGB camera. The images were used to determine lift-off length, temperature, and emissivity. The mathematical theory of two-color pyrometry and the calibration process used to measure the camera sensitivity is presented. The two most commonly used emissivity models in two-color pyrometry, the Hottel and Broughton and gray models, were investigated to determine which was the most appropriate for use in an oxy-coal flame.

A significant difference of 7% in the temperature and 24% in the emissivity results were found when processing an image with the Hottel and Broughton and gray emissivity models. The Hottel and Broughton model was selected for processing, because the Hottel and Broughton model is more appropriate for soot which appeared to dominate flame emissions. Using the two-color data, several trends were documented. Flame temperature was seen to decrease with increasing CO_2 flow rate. Within a given flame along the axial direction, temperature was seen to correlate with emissivity. As emissivity increased, flame temperature was seen to decrease. Many flames were lifted from the burner exit. Lift-off length was decreased and the flames became more attached by: 1) Increasing the amount of swirl given to the fuel stream, 2) Adding O_2 to the center primary tube or 3) Decreasing the flow of secondary CO_2. At higher center oxygen flow rates (above 8.5 kg/hr), the O_2 jet velocity was large causing increased entrainment and mixing which degraded burner performance.

ACKNOWLEDGMENTS

TABLE OF CONTENTS

LIST OF TABLES

LIST OF FIGURES

1   INTRODUCTION

The following section gives a brief background on the need for oxy-coal combustion research in the energy industry, a description of oxy-combustion and a summary of the research objectives in this work.

1.1   Background

Awareness of the environmental costs associated with energy production is increasing, as is the global demand for low-cost energy. The United States Energy Information Administration (EIA) reports that coal currently provides 45% of the electric power in the United States [1]. While the use of sustainable energy technologies is increasing, the demand for energy is increasing as well. The EIA predicts that electricity provided by coal will only drop by 2% by 2035, which will still constitute a net increase in coal derived power. Therefore, the vital role coal plays in energy production in the United States and the world cannot be immediately replaced with alternative energy sources. Research must be conducted to find ways to alleviate the environmental concerns associated with burning coal. The dangerous pollutants associated with coal combustion (NO_x, SO_x, Hg) are already regulated and the technology exists to keep those pollutant emissions below regulation limits. However, greenhouse gas emissions, particularly carbon dioxide (CO_2), have recently been defined as pollutants and will be regulated in the future. Ways to efficiently trap and sequester CO_2 are currently being explored. One

promising method enabling CO_2 capture is called oxy-combustion, in which fuel is burned in O_2 and re-circulated exhaust. This produces water (H_2O) and CO_2 as the two major by-products from which the CO_2 is easily extracted.

1.2   Oxy-combustion

Due to its prominence in energy production, coal-air combustion has been studied extensively; however, there is still much to learn about coal oxy-combustion. The substitution of CO_2 for nitrogen (N_2) as a diluent in the combustion environment changes the combustion process. When the nitrogen in air is replaced by the same concentration of CO_2, the temperature of the flame decreases due to the higher heat capacity of CO_2. Comparable heat transfer profiles occur when the oxygen concentration is around 30-35%, depending on the type of coal used [2]. Unlike air combustion, oxy-combustion allows the control of the oxidizer to diluent ratio. This ratio is manipulated by changing the amount of flue gas that is recycled in the system. Increasing the ratio can increase the speed of reaction and produce higher temperatures than in air combustion. The increased ratio could enable boiler size reductions and recycling the flue gas can cause a reduction in NO_x emissions. Retrofitting current air-combustion coal plants to oxy-combustion plants is possible [2].

Because heat transfer is the driving force behind energy production, the differences in heat transfer caused by the substitution of CO_2 for N_2 is of interest. Heat transfer is driven by temperature gradients; thus, one particular area of interest is to quantify the changes in the flame temperature when varying the oxidizer to diluent ratios. Quantifying these changes can be difficult. Thermocouples, suction pyrometers and laser optics are typical flame temperature diagnostics, but each presents challenges in use on oxy-coal flames. These challenges will be discussed further in Section 2.1. The technique used in this work to analyze the flame

2

temperature is two-color pyrometry. Two-color pyrometry is a non-intrusive diagnostic that can provide a two-dimensional mapping of temperature. Two-color pyrometry utilizes the emission from a surface or semi-transparent media at two wavelengths to calculate a temperature and emissivity. The quantification of the flame temperature and emissivity as a function of oxygen location, secondary CO_2 flow rate and swirl angle will be useful in characterizing oxy-combustion flames for practical applications.

1.3   Research Objectives

The objective of this work was to measure the flame temperature and visible band emissivity for a matrix of operating conditions. The matrix included combinations of three parameters. The parameters varied are summarized below in Table 1-1. The amount of oxygen put through the central tube of the burner was changed from 4-50% of the total oxygen supplied (42.71 kg/hr), or a mass flow rate of 1.7-21.4 kg/hr. Next, the amount of CO_2 added to the secondary stream as diluent was changed from 0-40 kg/hr. Finally, the swirl angle in the fuel stream was changed between three discrete angles: 0, 15 and 40°.

Concurrent with this work, other measurements were taken that are not included here [3]. The flue gas was analyzed with an FTIR to get NO values at each condition. Ash samples were collected to yield burnout data for each condition. All of these data were collected on the Brigham Young University (BYU) Burner Flow Reactor (BFR) with pure CO_2 used to simulate recycled flue gas.

Table 1-1. Summary of oxy-combustion conditions examined.

Parameter	Variation
Oxygen in Center Stream (kg/hr)	1.7, 4.3, 8.5, 12.8, 17.1, 21.4
CO_2 in Secondary Stream (kg/hr)	0, 10, 20, 30, 40
Swirl Angle of Fuel Stream (°)	0 , 15, 40

2   LITERATURE REVIEW

Currently, there is no inexpensive, simple, reliable way of taking temperature measurements in a particle-laden flame. Yet accurate temperature measurements are crucial in developing knowledge and expertise in combustion. Oxy-combustion produces a different composition of gases compared to air-fired combustion, and therefore can change the temperature and heat transfer profiles of the flame. The ability to reliably measure the temperature in an oxy-combustion flame is instrumental in developing this technology further. This section contains a review of potential temperature measurement methods for use in particle combustion, while investigating two-color pyrometry in depth, as that is the diagnostic used in this work. This section also contains a review of two emissivity models for their use in two-color pyrometry for coal combustion.

2.1   Measurement Methods

The following sections review temperature measurement options for coal-fired flames and the associated advantages and disadvantages of using these methods.

2.1.1   Thermocouples

Thermocouples are the most commonly used instruments for finding temperature in engineering applications. For particle-laden applications, there are multiple problems associated

with their use. Even costly, platinum-rhodium thermocouples have a temperature limit of 1450 °C, while combustion gas temperatures can be well over 2000 °C. Particle-laden flames can corrode and form deposits on thermocouple beads, thus reacting with the metal surfaces and producing noise and increasing error. Large thermocouple beads can be used to better enable their survival in the harsh combustion conditions, but this causes a slow response time and the thermocouple is more affected by radiation from the cooler reactor walls. Radiation corrections can be applied to thermocouples, but the uncertainty after correction can still be on the order of hundreds of degrees. Finally, thermocouples only provide a point measurement. A coal flame sheet constantly oscillates, moving the flame in and out of the thermocouple measurement volume; thus, the thermocouple does not read the flame temperature, but an average of the reactant and product gases.

2.1.2   Suction Pyrometers

Suction pyrometers, or high velocity thermocouples, are probes designed to pull a high velocity jet of gas past a shielded thermocouple. Suction pyrometers are the industry standard for combustion temperature measurements in spite of their numerous limitations. The probe and thermocouple must be must be built of expensive materials in order to withstand the high temperatures. Even when using high-cost materials, the temperatures still can exceed their melting point, especially during oxy-combustion. Due to the suction of particle-laden gas, the pyrometers often clog and cannot be used for long, continuous periods of time. The pyrometers require the use of a pump or high pressure gas or steam in order to produce the suction of gas past the thermocouple. This can be complex and expensive to implement. Like thermocouples, suction pyrometers provide single, point measurements. These measurements are spatially

averaged over the region from which the volume of gas is drawn into the pyrometer and temporally averaged over the response time of the shielding material.

2.1.3 Laser Optics

Complicated optical systems have been implemented to find the temperature in particle-laden flames. One such example is Coherent Anti-Stokes Raman Spectroscopy, or CARS. This method utilizes three lasers beams passing through the flame and being measured by receivers. CARS is expensive, difficult to operate, and potentially hazardous. The expense and complications of safety issues due to the use of a laser must be addressed in the system implementation. The solid particles in the flame often attenuate or scatter the laser beams, resulting in intermittent signals to the receivers [4]. This is especially true in large boilers where the laser beam has to travel over a longer length, rendering this method ineffective for large-scale measurements.

2.1.4 Two-Color Pyrometry

Two-color pyrometry is a non-intrusive diagnostic that can provide a two-dimensional mapping of temperature. Two-color pyrometry utilizes the emission from a surface or semi-transparent media at two wavelengths to calculate a temperature and emissivity. Two-color pyrometry has been used extensively in many combustion applications but its application is relatively new to coal flames. Reviews and discussions on the uncertainties of the two-color method for measuring temperature and KL can be found by Ladommatos and Zhao [5] and others ([6], [7], [8], [9]).

The signal for the two colors can be obtained by several methods. The simplest is to obtain emission from a single line of sight (provides a point measurement) which is split and

then optically filtered to produce two narrow bands of light. Shaw and Essenhigh [10] used this method on a laboratory scale reactor using pulverized coal to yield point temperature measurements. Lu and Yan [11] used a single, CCD camera to measure the two-dimensional (2D) temperature in a 500 kW pulverized-coal flame. The light from the flame was split and filtered into three narrow wavelength beams and captured by the CCD detector on the camera. The signals for the three beams were processed continuously to provide online temperature readings. The effects on temperature with varied air-fuel ratios, fuel flow rates, and particle sizes were examined. Huang et al. [12] used a similar method to yield 2D, continuous temperature measurements using a single CCD camera with rotating, narrow (10 nm) bandpass filters. Three hundred images were taken over a period of thirty seconds with each bandpass filter. The signals for each wavelength were averaged and then used to compute the average, 2D flame temperature.

Lou and Zhou [13] presented a novel use of RGB, CCD cameras to deduce the temperature distribution in a two-dimensional cross-section of a 300 MW, air combustion coal boiler. Four CCD cameras were mounted on a horizontal plane at four corners of the boiler and provided RGB video signals simultaneously. These signals were combined and transferred to a computer where the real-time flame images were displayed as an online, continuous output. The RGB data from the four cameras were used in a one-step, non-iterative calculation utilizing a modified Tikhonov regulatization method to produce the 2D flame temperature of the horizontal cross-section of the boiler. Since the calculation was one-step and non-iterative, the processing time was less than 2 seconds per image, which enabled this method to be used as an online temperature measurement.

Huajian et al. [14] implemented a system to deduce three-dimensional (3D) temperature distribution in a 660 MW furnace using twenty, RGB, CCD cameras. The system was validated

through the use of a portable, 2D pyrometry system using a single CCD camera and an infrared pyrometer. The portable system was considered validated by the infrared pyrometer with a difference in temperature readings of less than 7%. This difference was assumed to be caused by the increased radiation seen by the infrared pyrometer from the radiating combustion gases. Since the output of the portable system agreed well with the average temperature measurements from the 3D system at three different loads and along the height of the reactor, the 3D system was considered validated.

An innovative method for collecting two-dimensional, two-color images was developed by Lu et al. [15],where a single, RGB color, digital camera was used to filter the light and collect the image. An RGB camera uses a mask over a CCD array to allow a color band to reach adjacent pixies in the detector array. Three color bands are available: red, green, and blue. This method eliminates the need for an image splitter, a narrow band filter and multiple CCD arrays. The advantage of the RGB, two-color system is that it requires only a single camera and does not require additional optics. The disadvantage is that each color band is relatively wide (150-200 nm) compared to the narrow bands (1-25 nm) that can be selected when the image is split. The narrow band allows better separation between wavelengths and increases the sensitivity of the measured intensity ratio used to determine temperature. Narrow bands can also be selected to avoid interfering gases that may absorb light emission, while broad band measurements must assume the narrow bands of interference from radiating gases is negligible. As radiation from combustion gases primarily occurs in the infrared spectrum and this system only collects light from the visible spectrum, this assumption is considered valid ([13], [16]). The RGB, two-color method has been used to measure diesel flame temperatures [17], burning black liquor flame temperatures [18], burning biomass particle temperatures [11], coal circulating fluidized bed

temperatures [19], and pulverized-coal flame temperatures ([20], [21], [22]). References [20]-[22] present data taken in the same combustion facility with the same reactor and burner as used in this work. Both papers by Xue et al. ([20], [21]) investigate the effect oxygen location and secondary CO_2 has on NO production, while the second paper [21] also investigates loss on ignition data to examine the effect these parameters had on burnout. The results presented by Draper et al. [22] primarily investigate the effect two different emissivity models had on the temperature output of the RGB, CCD, two-color method and are heavily cited in this work. The equipment used by Svensson [23] to find the temperature and KL value of diesel flames was used with slight modifications for this work.

2.2   **Emissivity Model**

One of the unique challenges of implementing the two-color method to measure temperature in a coal flame is the variety of emitters present and the difficulty in inferring temperature from different emission sources. Visible emission from coal flames can originate from various particles, including coal, char, ash, and soot. The gas phase can also contribute significantly in the infrared spectral region. Soot particles are highly absorbing and emitting and relatively small quantities can be expected to dominate emission. However, soot is found in much smaller volume fractions ($\sim 1 \times 10^{-7}$) in coal flames ([24], [25]) than in normal diffusion flames ($\sim 1 \times 10^{-6}$). Soot will also burn out before char burnout is complete. Therefore, at some locations in a coal flame, soot emission should dominate, while at other locations, emission will be dominated by the gas phase. Visible flame emissions are more likely to be dominated by soot. Fletcher et al. [26] shows that soot is a significant if not dominant emitter in the near burner region of coal flames. Brown and Fletcher [27] conclude that the emission from soot particles

can be responsible for a decrease in flame temperature by as much as 300 K, transporting on the order of 10-15% of the total fuel energy out of the flame.

Individual soot particles are too small (20-40 nm) to be imaged, but the resultant cloud of soot particles produces a semi-transparent media with an associated equivalent emittance. Soot agglomerates may reach 1-2 μm but are still too small to be imaged individually. Coal, char, and ash particles are larger (2-500 μm). Some of the larger particles may be imaged individually and produce a surface temperature, but most of these particles will also participate as a semi-transparent media. Kerker [28] shows that in the Rayleigh limit, when particles are small relative to the wavelength of light, the absorption of light is inversely proportional to wavelength. For larger particles – those greater than the wavelength of light – all visible wavelengths of light will be absorbed equally. This means that clouds of small particles (soot) will absorb visible light preferentially according to wavelength, while larger particles (coal, char and ash) will absorb visible light equally at all wavelengths (gray emissivity). Since emissivity is related to absorption by Kirchoff's law, soot emissivity is spectrally dependent, while coal, char, and ash emissivities are spectrally independent or constant.

Hottel and Broughton [29] created a mathematical model that has been used extensively to describe the spectrally dependent emissivity of soot particles. Burning coal, char, and ash particles have been shown by Tree and Peart [24] to transmit visible light equally and thus emit light as a spectrally independent, or gray, body. The coal flame is therefore expected to produce particles that are both spectrally dependent and gray emitters.

Since it is not possible to determine the quantity of radiant emission that originates from soot in comparison to coal, char and ash in a coal flame, an appropriate model for emissivity is difficult to identify. Yet, an emissivity model is necessary for the implementation of two-color

pyrometry. Two approaches are prominent in the literature. References [10], [12], [13], [14], [15], [16], [18], [19], [30], [31], [32] assumed gray radiation in their measurements. One research group used the spectrally dependent Hottel and Broughton [29] emissivity model for soot ([11], [33]). In one case, temperature and KL images of a coal flame were determined using a mixture of both emissivity models. Lu et al. [34] used a gray assumption to determine temperature and then the Hottel and Broughton model was used to determine emissivity. Shaddix and Molina [35] imaged single particles of two different coals at various oxidizer-to-diluent ratios using single-color pyrometry which assumes blackbody radiation. No previous work regarding two-color measurements in coal flames has compared the difference in resulting temperature produced by assuming different emissivity models.

3   BACKGROUND

This section provides a detailed description of the theory behind two-color pyrometry and the calibration of camera for use in an oxy-coal flame. Specifically, the calibration section discusses the flatfield correction for the camera and calculating the spectral and non-spectral calibration arrays.

3.1   Two-Color Pyrometry Theory

Two-color pyrometry uses the intensity of two measured wavelengths of light to determine a temperature. In this case, a digital Red, Green, Blue (RGB) color camera was used to collect the intensity of two color bands that were used to infer temperature. An RGB digital camera works by utilizing a color mask that is placed on top of a two-dimensional array of detectors or charge-coupled device (CCD). The mask limits the light reaching a given detector, or pixie, to a color band of red (550-750 nm), green (400-650 nm), or blue (400-550 nm) as seen in Figure 3-1. The Bayer Pattern (Figure 3-2) is the most common arrangement of pixies used in color cameras consisting of a set of four pixies, 1 red, 2 green and 1 blue, which combine to make a single pixel.
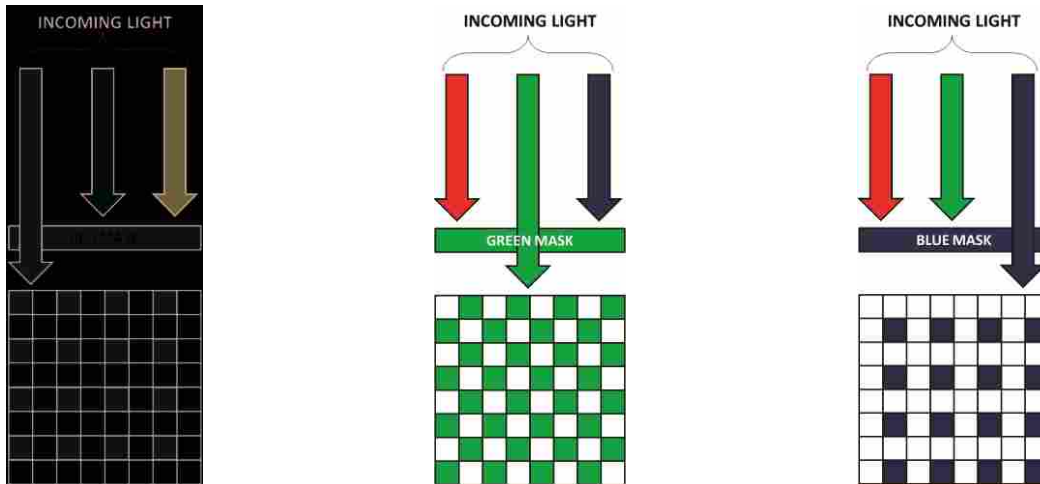
Figure 3-1. Visualization of the RGB color mask.
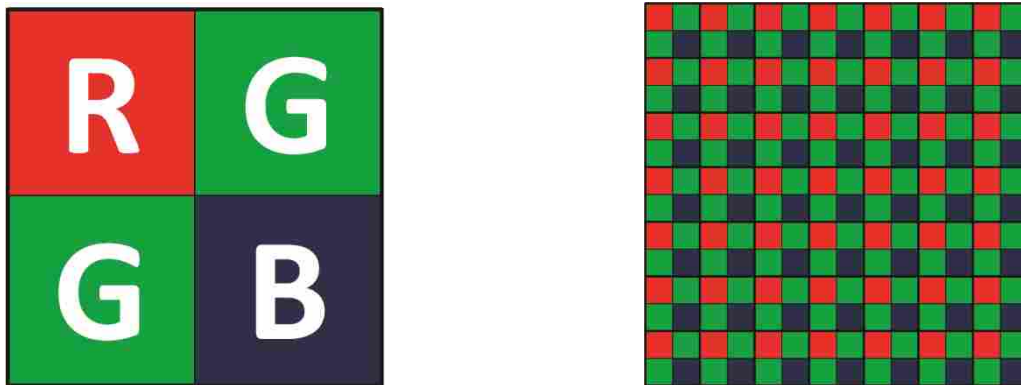
Figure 3-2. Left: Individual pixel composed of four pixies arranged in the Bayer Pattern; Right: Representation of a CCD array that utilizes the Bayer Pattern.

In contrast to narrow band pyrometry, which uses wavelength narrow bands of 1-25 nm, an RGB camera record color bands with a width of 150-200 nm. The narrow band approach can provide greater accuracy when the bands are properly selected to produce a maximum intensity ratio without gas interference, but the RGB method allows a two-dimensional image to be collected with a single camera and without the complex optical setup needed for narrow band, two-dimensional pyrometry. The UNIQ camera software, XCAP, allows the voltage of each pixie in the CCD array to be recorded separately to a digital array file without filtering.

A calibration must be done which relates the measured voltage of each pixie to a known intensity. This is complicated by several issues including: the spectral sensitivity of each pixie, the achromatic nature of lenses used to create the image, and the position specific transmittance characteristics of the optical path. A calibration technique was completed by Svensson et al. [17] and Svensson [23] for use on a diesel flame. The method involved the use of a blackbody, a monochrometer and a flat field image. The calibration of the camera has been repeated for this work in order to account for any changes in the camera and optics over time. Once calibrated, the intensities of each pixel can be used to infer temperature and emissivity. The details of the calibration method and a detailed discussion of uncertainty related to CCD arrays can be found in Svensson [17]. A review of the calibration method is provided here.

Figure 3-3 shows a cross section of the reactor with a simplified flame. The reactor walls are assumed cold, the flame has an assumed uniform depth of L and the position within the flame is measured by s, starting at the flame edge on the far side of the open port. The spectral intensity of the flame at distance L is the intensity transmitted through the optical train to the CCD camera.
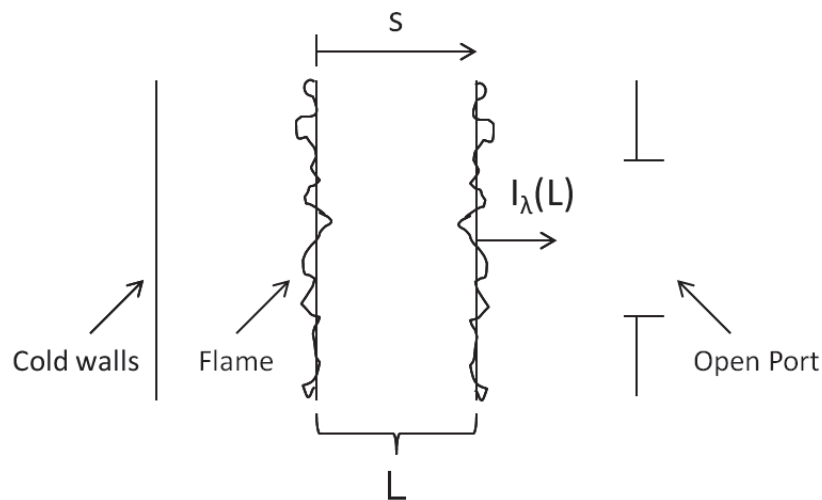
Figure 3-3. Cross section of reactor with simplified flame.

Assuming the flame is non-scattering [36], its spectral intensity is defined by the following version of the radiative transfer equation.

$$I_\lambda(\tau_\lambda) = I_\lambda(0)\exp(-\tau_{\lambda,s}) + \int_0^{\tau_{\lambda,L}} I_{\lambda,b}(\tau_{\lambda,s}')\exp-(\tau_{\lambda,s} - \tau_{\lambda,s}')\,d\tau_{\lambda,s}' \qquad (3\text{-}1)$$

The term I_λ is the spectral intensity ($\text{Wm}^{-2}\text{sr}^{-1}\mu\text{m}^{-1}$) and the term $I_{\lambda,b}$ is the blackbody spectral intensity as defined by Planck's distribution ($\text{Wm}^{-2}\mu\text{m}^{-1}$) as shown belong in Equation (3-2).

$$I_{\lambda,b}(\lambda, T) = \frac{C_1}{\pi\lambda^5\left(exp\left(\frac{C_2}{\lambda T}\right) - 1\right)} \qquad (3\text{-}2)$$

The term, τ_λ, in Equation (3-1) is known as the optical depth based on absorption and is defined by Equation (3-3), where κ_λ is the extinction coefficient (m^{-1}) and s is the distance along the line of sight within the flame (m) as shown in Figure 3-3.

$$\tau_\lambda = \kappa_\lambda s \qquad (3\text{-}3)$$

The term, $\tau_{\lambda,L}$, in Equation (3-1) is optical depth based on absorption of a flame of thickness, L, as defined in Equation (3-4).

$$\tau_{\lambda,L} = \kappa_\lambda L \qquad (3\text{-}4)$$

The boundary condition required to solve Equation (3-1) is presented in Equation (3-5). The spectral intensity along the line of sight on the far side of the open port (at s=0) is assumed to be zero. This means that radiation from the reactor walls is assumed to be negligible. In order to confirm this assumption, images were taken of the reactor walls after reaching steady-state temperature with no flame present. The intensity seen was negligible at the camera settings used to take the flame images.

$$I_\lambda(0) = 0 \tag{3-5}$$

Using this boundary condition, the solution of the radiative transfer equation is:

$$I_\lambda(\tau_{\lambda,L}) = I_{\lambda,b}[1 - \exp(-\tau_{\lambda,L})] = I_{\lambda,b}[1 - \exp(-\kappa_\lambda L)] \tag{3-6}$$

Based on Equation (3-6), the spectral, directional emissivity along the line of sight normal to the flame may be defined as:

$$\varepsilon_{n,\lambda} = \frac{I_\lambda(L)}{I_{\lambda,b}} = 1 - \exp(-\kappa_\lambda L) \tag{3-7}$$

In previous flame measurements where soot was the primary source of absorption, the extinction coefficient was approximated by the following Hottel and Broughton model [29], which is found in Equation (3-8). This model has been shown to be valid over the visible spectral range using the constant $\alpha = 1.39$ with the wavelength, λ, expressed in nm.

$$\kappa_\lambda = K/\lambda^\alpha \tag{3-8}$$

Thus, the spectral intensity of a flame of thickness, L, can be described as:

$$I_\lambda(L) = I_{\lambda,b}[1 - \exp(-KL/\lambda^\alpha)], \tag{3-9}$$

where the product KL is independent of wavelength.

As seen in Figure 3-4, the spectral intensity from the flame first passes through a neutral density filter. The neutral density filter was used to keep intense light from saturating the camera and its spectral transmittance is the calibration array, ς_λ. The light then passes through a sapphire window, external IR filter, camera lens, internal IR filter and onto the CCD detector array. The sapphire window was included because it was a necessary part of the optical path in other experiments where the same calibration was used. The two IR filters limited the upper range of

wavelengths (750 nm) to the visible region where the Hottel and Broughton emissivity model is applicable. The term $\beta_{\lambda,i}$ accounts for the spectral transmittance for each color of the remaining components in the optical array as well as the spectral response of the detector. Thus, the spectral intensity incident on the detector can be described by the following equation:

$$I_{\lambda,i,d} = I_\lambda(L)\varsigma_\lambda\beta_{\lambda,i}. \tag{3-10}$$
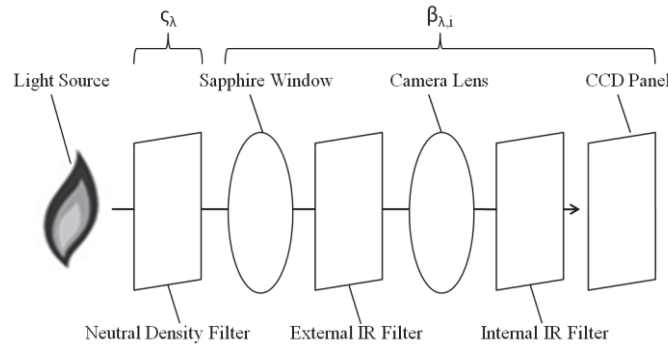
Figure 3-4. Optical path of light from flame or blackbody cavity to CCD panel.

The spectral irradiation incident on the detector is given by:

$$G_\lambda = \int_{2\pi} I_{\lambda,i,d} \cos(\theta)\, d\Omega. \tag{3-11}$$

The spectral intensity incident on the detector is zero unless the solid angle, $\Delta\Omega$, is the solid angle subtended by the lens as viewed from the detector, $\Delta\Omega_{d\rightarrow lens}$. Since the solid angle subtended by the lens as viewed by the detector is small and $\theta\sim0$ within the solid angle of the lens:

$$G_\lambda \cong I_{\lambda,i,d}\Delta\Omega_{d\rightarrow lens}. \tag{3-12}$$

The pixel count, P_i, is the detector response for each color at each pixel. It is proportional to the total amount of radiation energy incident on the detector. The amount of energy changes not only with differing amounts of irradiation from the flame but also with the length of the

exposure time, t, and the aperture area, A, used. The integration band from λ_1 to λ_2 represents the wavelength endpoints of the visible spectrum, 400-815 nm.

$$P_i = \tilde{s}_i \int_{t_1}^{t_2} \int_{A_d} \int_{\lambda_1}^{\lambda_2} G_\lambda \, d\lambda \, dA \, dt, \tag{3-13}$$

Substituting s_i for $\tilde{s}_i \Delta\Omega_{d \to lens}$ and Equations (3-2), (3-9), (3-10) and (3-12) into Equation (3-13) gives the governing equation that relates the pixel count to the unknown temperature and KL values of the flame:

$$P_i = s_i \int_{t_1}^{t_2} \int_{A_d} \int_{\lambda_1}^{\lambda_2} \left[\frac{C_1}{\pi\lambda^5 \left(exp\left(\frac{C_2}{\lambda T}\right) - 1 \right)} \right] \left[1 - \exp\left(-\frac{KL}{\lambda^\alpha} \right) \right] \varsigma_\lambda \beta_\lambda \, d\lambda \, dA \, dt. \tag{3-14}$$

This model now allows for the solution of temperature and KL at each pixel. The two values are found using the MATLAB function "fsolve," which can solve systems of non-linear equations. First, an initial guess for T and KL is given. Then, Equation (3-14) is integrated numerically twice, using the red and blue pixel values, the initial guesses and the calibration arrays. The process is iterated until the function converges upon values for T and KL that solve both the red and blue versions of Equation (3-14). The solution for KL, which is wavelength independent, can then be used to determine the spectral, directional emissivity normal to the flame using Equation (3-7). The visible band emissivity (from 400-815 nm) is found using Equation (3-15).

$$\varepsilon_{n,band} = \frac{\int_{\lambda_1}^{\lambda_2} \varepsilon_{n,\lambda} I_{\lambda,b}(T) d\lambda}{\int_{\lambda_1}^{\lambda_2} I_{\lambda,b}(T) \, d\lambda} \tag{3-15}$$

3.2   Calibration

Calibration of the camera for temperature and emissivity measurements requires that the voltages from each pixel in the CCD array be related to a known incident amount of energy. The

calibration process involves first determining the flat field correction; second, determining the transmittance and spectral response of the optical path [$\beta_{\lambda,i}$ and ς_λ in Equation (3-11)]; lastly, determining the sensitivity or voltage per unit incident energy produced for each pixel [s_i in Equation (3-11)]. The flat field correction and each of the calibration constants were determined during previous experiments where they were used to measure temperature and emissivity in a diesel flame [17]. While the details of the calibration and uncertainties involved with CCD measurements can be found in Svensson [23] and Svensson et al. [17], the calibration processes will be briefly reviewed here with a detailed analysis and presentation of how new s_i values were calculated for this research in coal flames.

3.2.1   Flat Field Correction

The use of an aperture and lens to image light produces a non-uniform distribution of that light on the CCD array. The distortion increases with increasing aperture size. In order to obtain quantitative measurements, the extent of the distortion must be quantified for each aperture.

The flat field correction obtained by Svensson [23] was determined by exposing the camera to a diffuse sheet of glass illuminated by the sun. An example of a flat field image is shown in Figure 3-5 with the intensity along the horizontal line shown in Figure 3-6. The dark red color shows the largest intensities towards the middle of the array with a sharp drop-off at the edges. Multiple images were averaged at each aperture setting and normalized by the highest value in the array to produce the flat field image for each aperture.
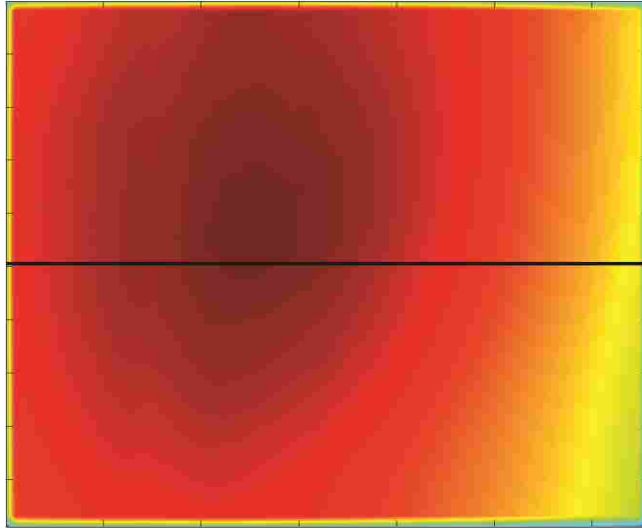
Figure 3-5. Color contour plot of pixel response to a uniform light source.
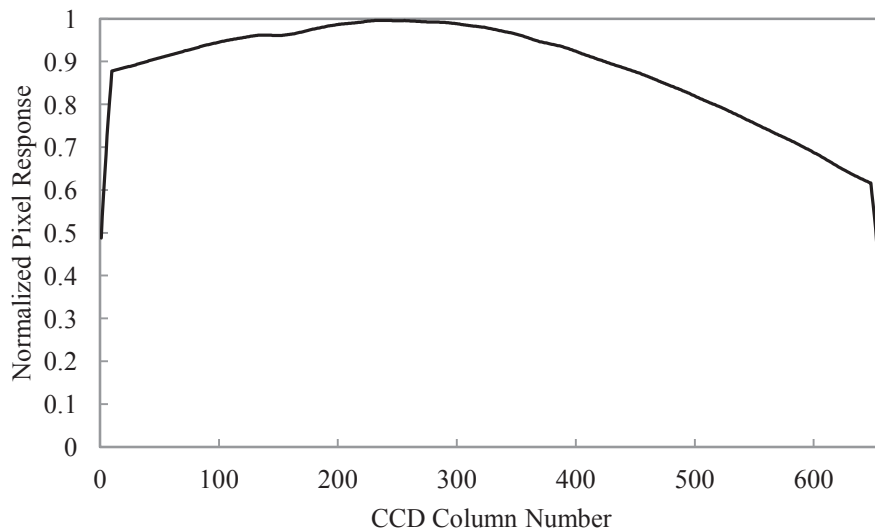
Figure 3-6. Center line of pixel response to a uniform light source as function of CCD column number.

3.2.2 Spectral Response Calibration

The spectral response of the optical system, $\beta_{\lambda,i}$, is a combination of the transmittance of the lenses and filters and the spectral response of the detectors on the CCD array. The spectral response function was obtained by imaging a blackbody of known temperature through a

monochromator. The monochromator separated the light from the blackbody into 5 nm bands throughout the visible range of the spectrum between 400 and 815 nm. The results shown in Figure 3-7 from Svensson et al. [17] show the largest separation in spectral transmittance is between the red and the blue wavelength bands while green is in the center and overlaps both of the other colors.
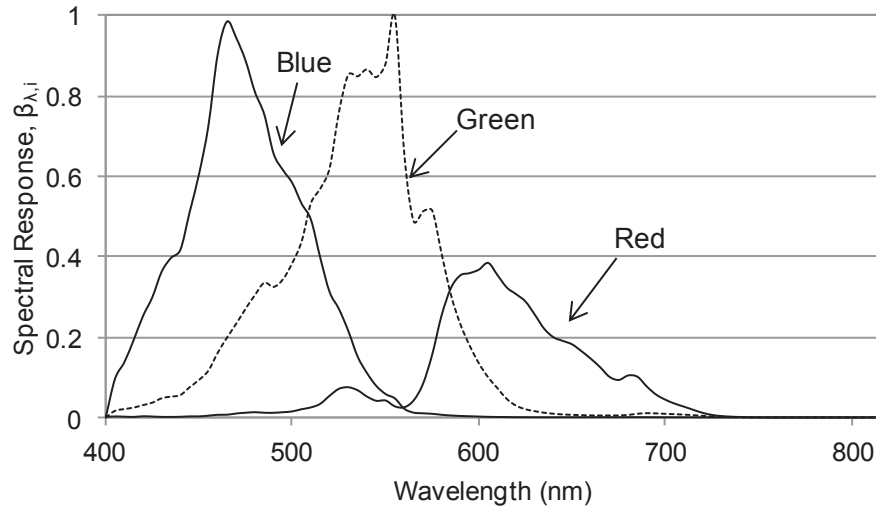
Figure 3-7. RGB spectral response as a function of wavelength.

3.2.3   Spectral Transmittance Calibration

Various neutral density (ND) filters were used to reduce the amount of light going into the camera and allow the imaging of high intensity flames. For the results presented in this thesis, only one filter was needed, which attenuated 90% of the light from the flame. However, filters that had 0, 50, 70, 99 and 99.9% attenuation were also calibrated to be used if necessary. The calibration array of the spectral transmittance of the ND filters, ς_λ, is plotted as a function of wavelength for all the filter options in Figure 3-8. These values were also measured by Svensson et al. [17] and agree with the published transmittance data accompanying the filters. The attenuation is fairly constant over the visible wavelength region.
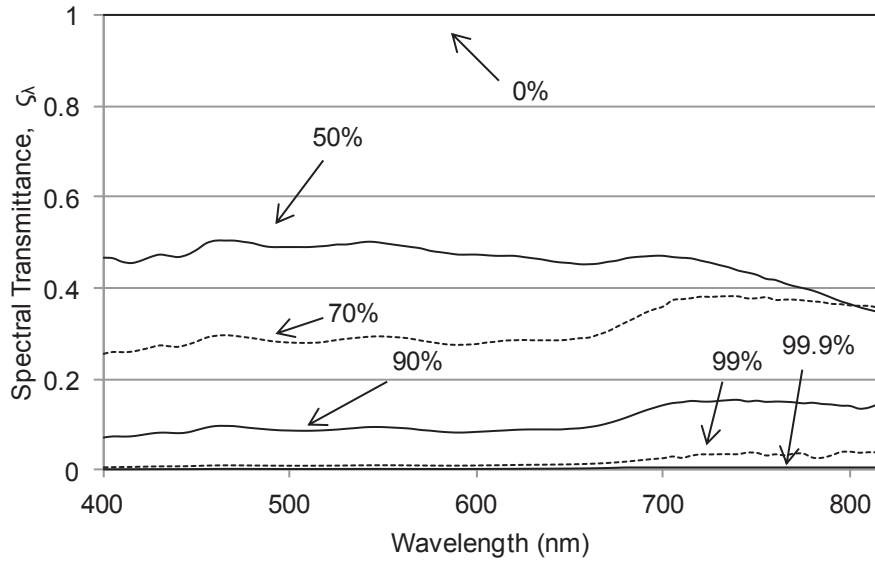
Figure 3-8. Spectral transmittance of neutral density filters as a function of wavelength.

3.2.4   Determination of Non-Spectral Terms

The three non-spectral terms in the governing equation **Error! Reference source not found.** are:

t, the exposure time, A, the aperture area vector, and s_i, the sensitivity constant for each color. These values can be found with a blackbody generator, which produces light at a known temperature and emissivity. With a source of known emission, the integral over the visible wavelength band for each color is known and can be abbreviated as E_i and is seen in Eq. (3-16). This leaves the effects of the exposure time, aperture area and the sensitivity constant as the only unknowns.

$$P_i = E_i \int_{t_1}^{t_2} s_i \, A \, dt. \qquad (3\text{-}16)$$

The sensitivity constant correlates the total incident energy with the resulting pixel response for each color. However, changing exposure times and aperture settings changes the pixel response even when the total intensity from the light source remains constant. These parameters must be allowed to change to allow flexibility in taking data from flames of different

intensities. There is a narrow range of pixel response values that provide useful data; if the image is too dark, the response for the blue will be too low and, if the image is too bright, the response for the red will become saturated and unusable. Therefore, changing the combination of aperture settings and exposure times allows the user to get the best signal possible at flames of varying intensities. The pixel response is the charge produced on the CCD panel that is digitized into discrete integers ranging from 0 to 1023.

In order to determine the unknowns, t, A and s_i, images were taken of the blackbody at six intensities (blackbody temperatures), four aperture settings and up to fourteen exposure times as seen in Table 3-1. At each combination of the three parameters, three images were taken. Once these images were processed for their pixel response, any that were too dark or saturated were discarded. The same 50x50 square of pixels was analyzed at the center of each image (Figure 3-9). The pixel responses after flat field correction within this square were extracted and averaged. This process was done for each of the three images taken at each setting to reduce random error as much as possible. The pixel responses reported are the averages of the three values.

Table 3-1. Matrix of blackbody cavity and camera settings used to obtain blackbody calibration images.

Temperature (°C)	Aperture Setting	Exposure Time (msec)
1400, 1450, 1500, 1550, 1600, 1650	8, 10, 12, 14	0.016, 0.032, 0.050, 0.067, 0.083, 0.100, 0.125, 0.167, 0.200, 0.250, 0.500, 1, 2, 4

Table 3-2 is a matrix of selected blackbody images. Each row displays images taken at a particular exposure time and each column displays images taken at particular blackbody temperature. All the images were taken at an aperture setting of 14, meaning the lens was fully

open. As expected, the visible intensity from the blackbody increases with increasing temperature and increasing exposure time.
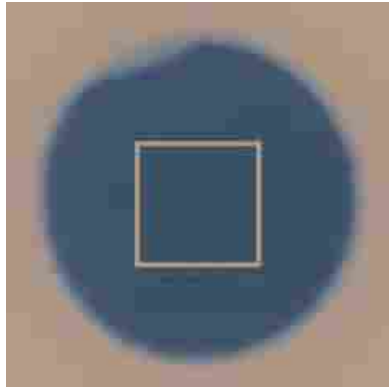
Figure 3-9. Illustration of pixel area analyzed in blackbody images.

Table 3-2. Matrix of selected blackbody calibration images.

At a fixed exposure time and aperture setting, the pixel response was compared to the incident energy received from the blackbody by changing the blackbody temperature as is shown in Figure 3-10. The figure shows that the response of the camera is linear with incident energy from the blackbody emission. It should be noted that the following discussion provides results

24

for the red pixels only but the same procedures were taken with the blue and green pixies. These results are not shown for the sake of brevity.
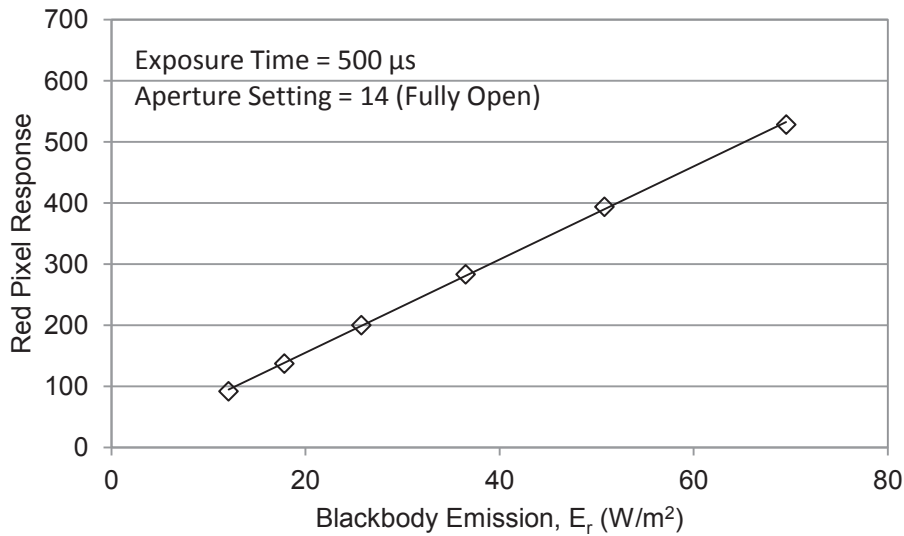
Figure 3-10. Red blackbody emission versus red pixel response at exposure time of 500 μs and fully open aperture setting (14).

3.2.4.1 Initial Energy Correction

Figure 3-11 below shows the pixel response versus exposure time for the four aperture settings used in the calibration. These data were taken at single blackbody emission setting at a temperature of 1650 °C. Best fit lines were drawn through each aperture data set. This figure shows again that the detectors in the camera are linear with incident energy. In this example the energy is changed by changing exposure time rather than changing blackbody emission intensity. In this case, the pixel response produced R^2 values of 0.99+. However, the best fit lines do not intersect at the origin as expected. This can be seen more clearly in Figure 3-12, which focuses on the short exposure times near the origin. In this figure, the best fit lines are extended past the smallest exposure time as dotted lines until the lines hit the x-axis.

25
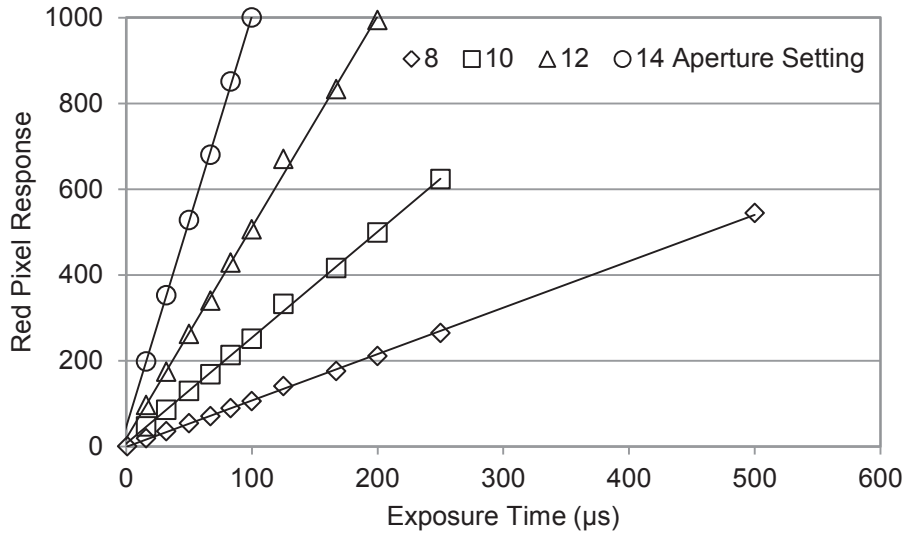
Figure 3-11. Red pixel response as a function of exposure time at a temperature of 1650 °C.
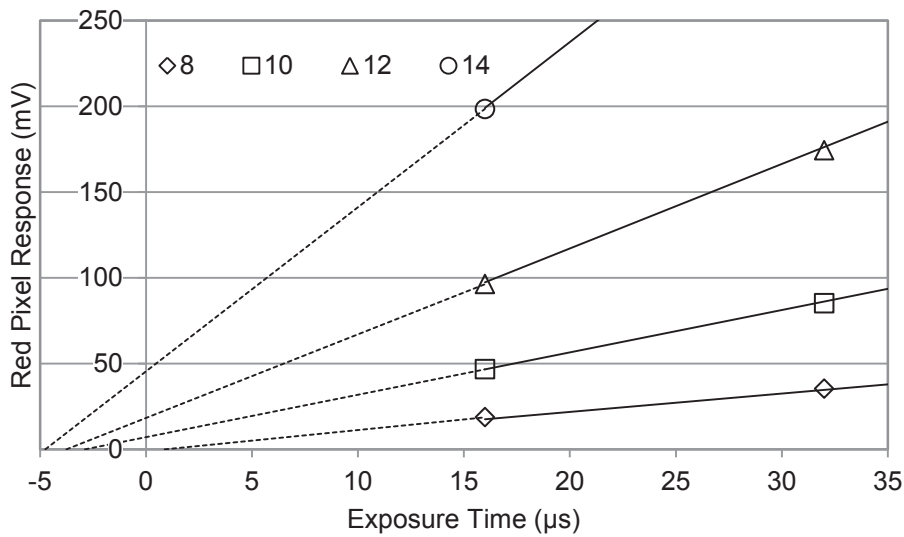
Figure 3-12. Red pixel response for short exposure times at a temperature of 1650 °C. Dotted lines extrapolate best fit lines back from shortest exposure time at each aperture setting.

As can be seen, the x-intercept is not the same for each line indicating that a single offset or error in the exposure time is not the cause for the lines not intersecting the origin. It can be seen that the y-intercept is near zero for small apertures areas (low incident intensities) and becomes increasingly positive for the large aperture areas (high incident intensities). This offset

needed to be characterized and included in the calibration for this applications because oxy-flames produce high intensities and require images be taken at the shortest exposure times of the camera where this offset becomes a significant source of error.

The observed behavior near the origin suggests the y-offset is a function of incident intensity or rate of energy flux, not total incident energy. The digital camera does not employ a physical shutter that blocked light to the detectors before an image was taken. Instead, each photo-detector in the array continuously collects charge from incident light. The camera "shutters" the light by grounding the detectors and thus removing charge until an image is to be collected. The charge then builds over the exposure time until it is collected or read from the detector array. One possible explanation for the observed results showing a positive y-intercept is that there is a small resistance between the detectors and ground such that, at steady state, before the camera triggers the collection of charge for an image, the detector contains a small charge proportional to the incident flux of energy.

Whether or not this is the cases, a mathematical description of the observed behavior was constructed as shown in Equation (3-17), where P_i is the pixel response, m_i is the slope of the best fit line, such as the lines in Figure 3-11 (μs^{-1}), t is the exposure time (μs) and b_i is the y-intercept. The slope, m_i, is a function of the incident intensity on the CCD panel; as the incident intensity increases, the slope also increases. The intercept, b_i was modeled as being proportional to the incident intensity (m_i) with an offset of c_i. The values of k_i and c_i were determined by a least squares best fit to the measured data. The results are summarized in Table 3-3.

$$P_i = m_i t + b_i = m_i t + (k_i m_i + c_i) \tag{3-17}$$

Since the y-intercept b_i was a bias existing on the array before an image was taken, it was subtracted from the measured pixel count in order to produce a corrected pixel count representing only the energy collected during the exposure time.

$$P_{i,corr} = P_i - b_i \tag{3-18}$$

Table 3-3. Summary of k_i and c_i.

Red		Green		Blue	
k_r (µs)	c_r	k_g (µs)	c_g	k_b (µs)	c_b
5.258	-11.065	6.042	-5.097	15.481	-2.475

Once k_i and c_i were found, the offset for each pixel in a flame image at unknown intensity could be found. First, the governing equation, Equation (3-17), was solved for m_i:

$$m_i = \frac{P_i - c_i}{t + k_i}. \tag{3-19}$$

These values are all known: k_i and c_i from the calibration above in Table 3-3, t is the known exposure time used to take the image, and P_i is the output pixel response from the camera. Once m_i is known, b_i can be solved for using Equation (3-17) and the corrected pixel response can be found using Equation (3-18). This correction was done for each color on each pixel within the flame boundary in each image.

With the correction for the pixel response offset, the exposure time correlation is complete. The model to predict pixel response, as seen in Equation (3-17), adequately models the blackbody data. This can be seen in Figure 3-13, in which the blackbody data is plotted versus the predicted data. The data points follow the straight line with a constant slope of 1.00, which means the model accurately characterizes the data. Thus, the governing equation for calibrating the system becomes:

$$P_{i,corr} = E_i s_i A\, t, \tag{3-20}$$

where A and s_i still remain unknown.
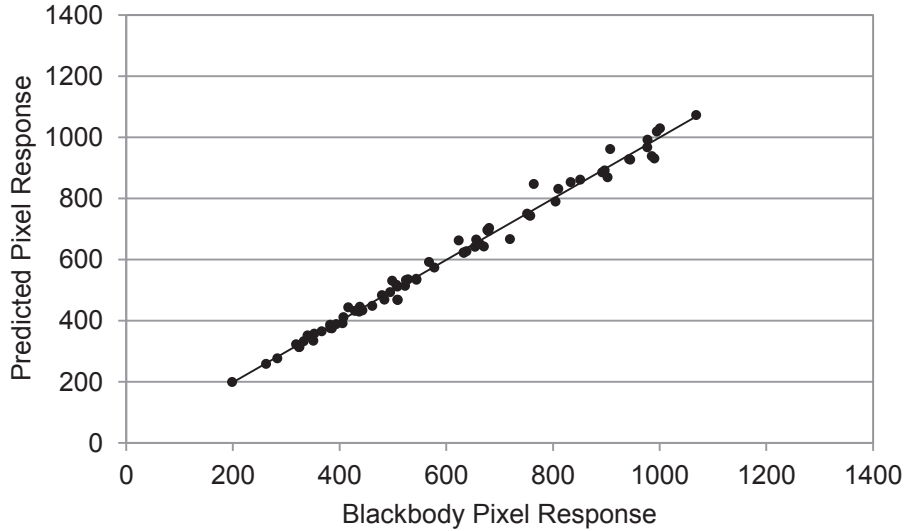
Figure 3-13. Blackbody pixel response as a function of predicted pixel response.

3.2.4.2   Aperture Setting Correction

The effect of aperture area on pixel response must also be characterized. At the aperture setting 14, which is the setting in which the lens is fully open, the area of the lens is a circle with a diameter of 1.7 cm and thus an area of 2.262×10^{-4} m^2. As the aperture settings decrease, the lens closes, and the aperture area gets smaller. However, the shape is not perfectly circular. The area is reduced by closing three overlapping fins and cannot be easily measured. Thus, the aperture area at each setting must be calculated with the blackbody pixel response data. The pixel response is linear with both exposure time and blackbody emission. Figure 3-14 plots every red blackbody pixel response versus the blackbody emission multiplied by the exposure time. Without aperture settings taken into account in x-axis calculation, the data is linear but remains in 4 different lines.

29
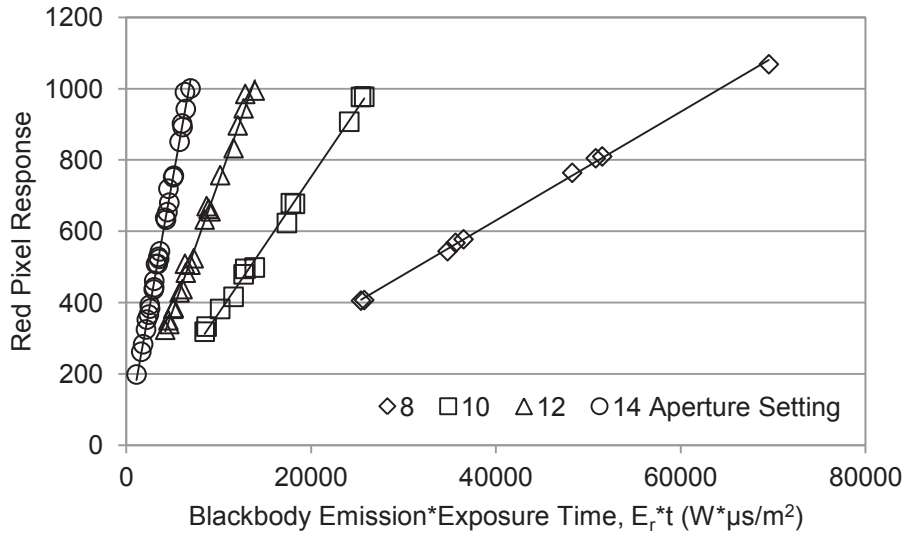
Figure 3-14. Red pixel response versus the blackbody emission multiplied by the exposure time for four aperture settings.

An aperture vector can be calculated to correlate the area of the aperture at each setting. Once this is found and included in the x-axis calculation, it collapses the four lines into one as seen in Figure 3-15.
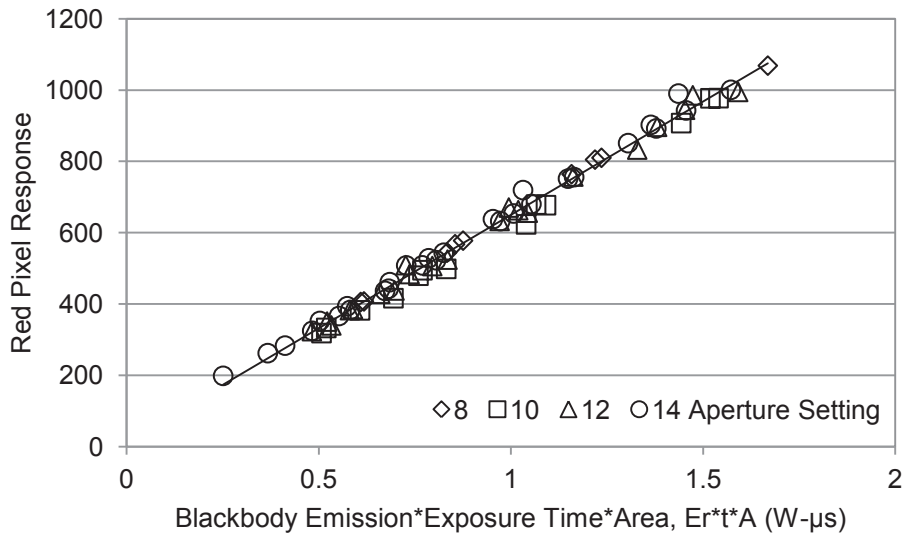
Figure 3-15. Red pixel response versus the blackbody emission multiplied by the exposure time and the aperture area.

This calculation was done by taking all the data points at the 14 aperture setting and plotting them versus the blackbody emission multiplied by the exposure time and the area of the fully open lens (2.262×10^{-4} m^2). This produced the hollow circle data series in Figure 3-15. The data for the 8, 10 and 12 aperture settings were multiplied by various constants until they collapsed onto the same line as the 14 aperture setting. The constant that caused each series to follow the 14 aperture series the closest is the area in m^2 of the aperture at that setting. These constants are summarized in Table 3-4.

Table 3-4. Summary of aperture vector values.

Aperture Setting	Aperture Area, A (m^2)
8	2.400×10^{-5}
10	5.983×10^{-5}
12	1.145×10^{-4}
14	2.262×10^{-4}

3.2.4.3 Sensitivity Constant

Once the effects the aperture area and the exposure time have on the pixel response are known, the sensitivity constant for each color can be found. It is the slope of the line in Figure 3-15 and it can be calculated by rearranging Equation (3-20).

$$s_i = \frac{P_{i,corr}}{E_i \, A \, t}.$$
(3-21)

The sensitivity constant was calculated at each blackbody data point and averaged for each color. The results are summarized in Table 3-5.

Table 3-5. Summary of sensitivity constant values.

s_r (W^{-1}-μs^{-1})	s_g (W^{-1}-μs^{-1})	s_b (W^{-1}-μs^{-1})
641.9	453.6	327.5

4 EXPERIMENTAL METHOD

This section describes the facilities and equipment used to conduct the experiments for this work. First, the reactor system and burner are described. Next, the ultimate and proximate analyses of the coal are given. These are followed by a summary of the flow rates for all conditions investigated in this work. Finally, a description of the camera used in the two-color pyrometry measurements is presented.

4.1 Reactor System

The pyrometry measurements were taken in the Burner Flow Reactor (BFR) at Brigham Young University (BYU). The BFR, shown in Figure 4-1, is a down-fired, pulverized coal reactor that was equipped with an Air Liquide, pipe-in-pipe, oxy-coal burner with a thermal input of 150 kW. The burner uses a pure CO_2 stream to convey coal and dilute the oxygen. The coal is fed by a screw auger, loss-in-weight, coal feeder. The BFR is a cylindrical vessel lined on the inside wall with refractory and with an outside wall that contains a water-cooled jacket. The reactor stands vertically at a height of 2.4 meters and an inside diameter of 0.75 meters. The bottom of the reactor tapers to a water-cooled exhaust pipe. The reactor is divided into six sections, each with separate water cooling. Each of the six sections has four access doors, any of which can be removed to view into the reactor. After the reactor wall temperatures reached steady state, a top door was removed from the reactor in order to take the pyrometry

measurements. The equipment setup is also shown in Figure 4-1. The camera (1) and various optical filters (2) were aligned on a steel plate and tilted upward to view into the reactor, yielding images of the base of the flame against the background of the relatively cool burner block. The camera was controlled by XCAP software from a personal computer (3). The view from the port is limited to the base of the flame extending approximately 25 cm axially downward.
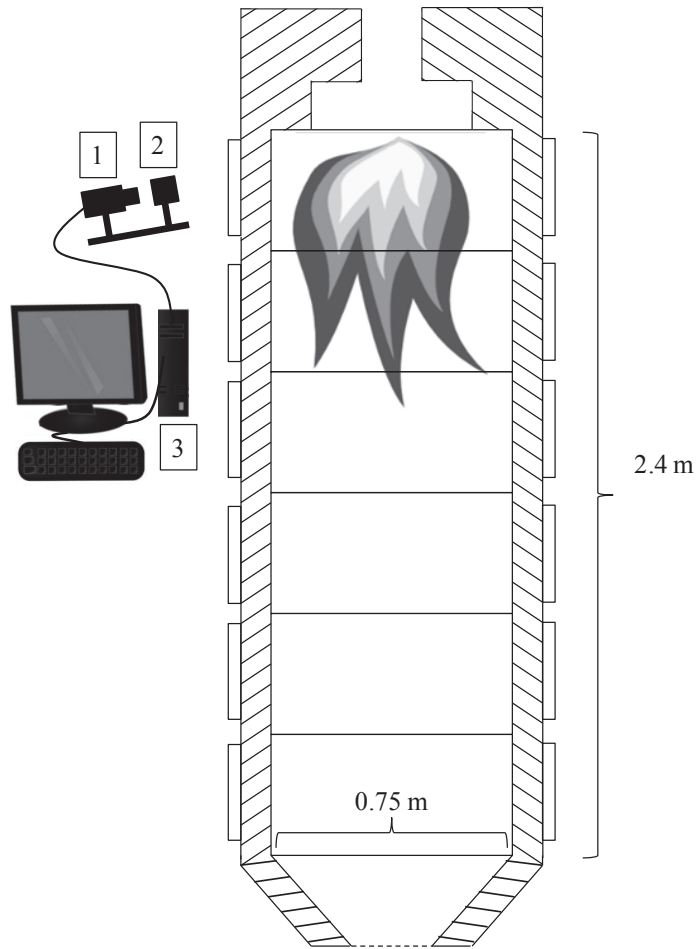
Figure 4-1. Equipment set-up and cross-section view of the BFR.

A sample line was connected to the water-cooled exhaust pipe for exhaust gas analysis from a Fourier Transform Infrared spectrometer (FTIR) and a gas chromatograph (GC). Also located downstream of the water-cooled exhaust pipe is a real-time O_2 sensor. The exhaust gas is

33

drawn through the reactor by an induction draft fan. The fan draws a constant volume flow rate of gas in excess of the reactor flow rate making the reactor pressure negative, but the pressure inside the reactor can be changed by adjusting a bypass valve. This valve allows the fan to draw room air as it is opened, making the pressure in the reactor positive. Typically when taking data, the reactor is maintained at a slightly positive pressure (0.5 inches H_2O) to avoid air entrainment in the reactor, which can change the stoichiometry of the flame. However, since the optical pyrometry measurement required the removal of a port, a positive reactor pressure would have caused dangerous product gases to spew into the room. Therefore, the reactor was kept at a slightly negative pressure when the pictures were being taken. The effect of this potential air entrainment into the reactor environment is discussed in Section 5.2.2.

The oxy-combustion burner is supplied with pure O_2 and CO_2 from large, 265 Liter tanks that hold liquid O_2 and CO_2. Figure 4-2 describes the experimental setup of the reactor. Oxygen flows from the tanks and passes through an ambient air vaporizer to warm it up to a gaseous state. Next, it is split into primary and secondary lines, each of which flow through a valve train. The valve train is described in detail by Zeltner [3]. It consists of a series of ball valves, solenoid valves, pressure gauges, check valves and mass flow controls, all of which contribute to control the flow and ensure that it is flowing safely. The primary stream is fed directly into the center tube in the burner and the secondary stream is fed to the outermost burner tube. The CO_2 follows a similar process. It flows from the tanks and into an electric heater to warm it to the gas phase. It is split into primary and secondary lines and then each line flows through a valve train similar to the oxygen valve train. The primary CO_2 line runs through the coal feeder to entrain the pulverized coal after which it flows into the fuel stream tube in the burner. The secondary CO_2

34

line runs into the same outer tube in the burner as the secondary O_2 line. A more detailed description of the burner is found in the following section (Section 4.2).
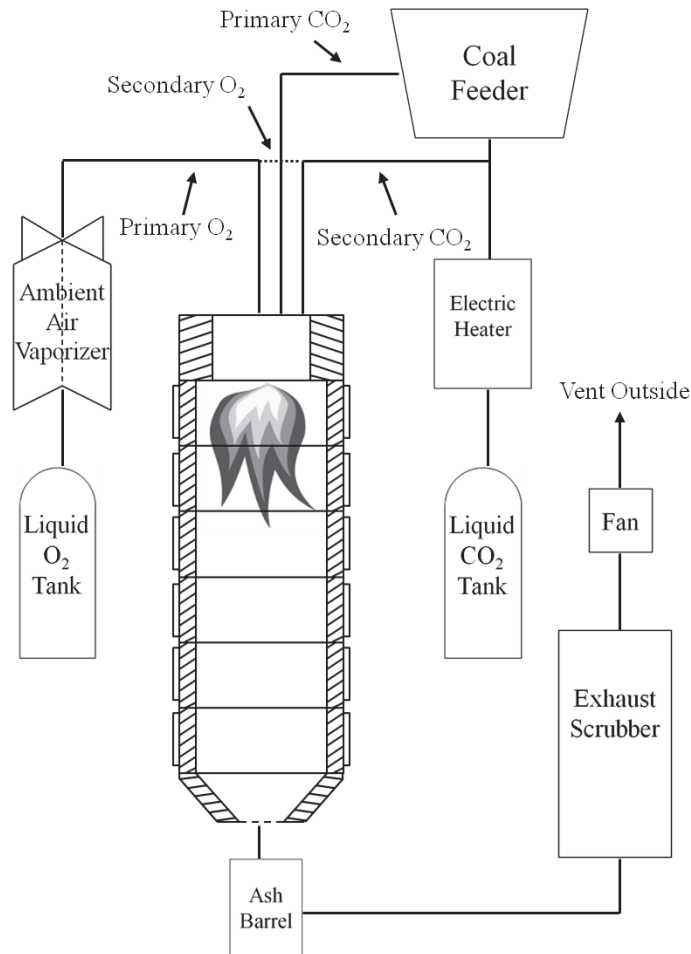
Figure 4-2. Experimental set-up of reactor.

4.2 Burner Description

The burner, designed and built by Air Liquide, is composed of two stainless steel tubes concentrically mounted which rest in a cylindrical block of refractory as shown in Figure 4-3. The refractory block contains a 10 cm recess and the two tubes are recessed a further 8.5 cm. The burner allows for the study of oxygen placement at high oxygen participation ratios (high O_2 to total gas concentrations). Figure 4-3 shows a cross-section schematic of the burner in the burner

block. Stream 1 is fed only by the pure oxygen and is referred to as the center oxygen stream. Stream 2 is fed by the primary CO_2 stream, which contains a mixture of pulverized coal and CO_2, and is referred to as the fuel stream. Stream 3 is fed by both the O_2 and CO_2 secondary streams, and is referred to as the secondary stream. The secondary stream always contains oxygen but adding CO_2 to this stream is optional. The center oxygen stream (1) and secondary stream (3) are not swirled, but the fuel stream (2) is swirled upstream of the exit. The swirl is created by attaching a swirl plate within the fuel stream annulus. In this work, different swirl plates of 15 and 40° as well as no swirl plate were investigated to see the effect of swirl on the flame properties.
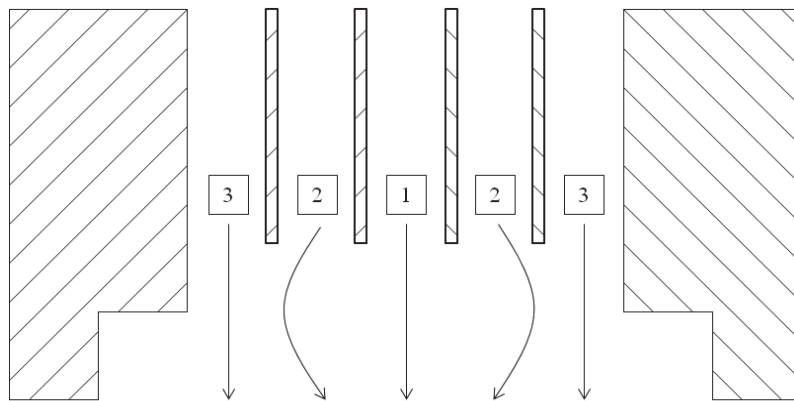
Figure 4-3. Cross-section of pipe-in-pipe, Air Liquide, oxy-coal burner; Stream 1 flows center oxygen; Stream 2 flows swirled coal and CO_2; Stream 3 flows secondary oxygen and optional secondary CO_2.

4.3 **Fuel, Oxygen and Diluent (CO_2) Flow Rates**

For all data presented, the reactor was run at a thermal value of 150 kW, or a constant coal feed of 18 kg/hr. The primary CO_2 stream, which carried the coal, was also kept constant at 25 kg/hr. The total amount of oxygen entering the reactor was also kept constant (42.71 kg/hr) to give an excess O_2 of about 4%. The two flow rate parameters varied were: the amount of oxygen split between the center oxygen and secondary streams and the addition of CO_2 to the secondary

36

stream. The flow rate of oxygen in the center tube was varied between 1.7-21.4 kg/hr. The lowest center oxygen flow rate was set to 1.7 kg/hr instead of 0 kg/hr to prevent any fuel/gas/particles from flowing up the tube and contaminating it. The amount of secondary CO_2 (CO_2-S) varied from 0-40 kg/hr. Since some oxygen was always flowing through the secondary stream, the secondary CO_2 could be set to zero. These sweeps were performed for three different swirl vane angles: 0, 15 and 40°. Table 4-1 summarizes flow rates for the various conditions investigated in this work. It should be noted that the secondary CO_2 sweep using no swirl vane is more limited. Since there was no swirl, high flow rates of secondary CO_2 caused the flame to detach and blow out, making it impossible to take data. Thus, thirty conditions were examined at the 15° and 40° swirl vanes and eighteen conditions were examined using no swirl vane.

Table 4-1. Matrix of flow rate conditions investigated in this work.

Swirl Vane Angle (°)	Coal (kg/hr)	Primary CO_2 (kg/hr)	Total O_2 (kg/hr)	Center O_2 (kg/hr)	Secondary CO_2 (kg/hr)
0	18.0	25.0	42.71	1.7, 4.3, 8.5, 12.8, 17.1, 21.4	0, 10, 20
15	18.0	25.0	42.71	1.7, 4.3, 8.5, 12.8, 17.1, 21.4	0, 10, 20, 30, 40
40	18.0	25.0	42.71	1.7, 4.3, 8.5, 12.8, 17.1, 21.4	0, 10, 20, 30, 40

4.4 Coal Analysis

The coal used in the oxy-combustion measurement was Flambant de Provence (Flambant) coal from France. The proximate and ultimate analyses are described in Table 4-2.

.

Table 4-2. Proximate and ultimate analysis of
Flambant de Provence (Flambant) coal.

	As Received, wt. %
C	73.81
H	4.12
N	1.15
S	0.90
O (by difference)	10.63
Ash	6.05
Moisture	3.34
Volatile Matter	34.64
Fixed Carbon	55.97
	Btu/lb
Heating Value (HHV)	13,353

4.5 Camera

A UNIQ, UC-600CL, 10-bit, RGB, CCD camera was used in conjunction with Version 3.7 of the EPIX computer program, XCAP, to capture the flame images. The program enabled camera exposure times ranging from 16-4000 μs. When taking the images, the gain must be adjusted to maximize the pixel values as much as possible without causing large numbers of pixels to saturate. This is often difficult, because the intensity of the flame can vary widely over its area. Often different settings were used to take data at the same condition and then analyzed later to see which gave the most useful pixel response. The gain was adjusted by typically adjusted by changing the exposure time but could also be adjusted by changing the aperture setting and neutral density filter as well. Due to the high intensity of the flames, the images were taken at the shortest exposure times, ranging from 16-100 μs. The XCAP program enabled the pictures to be saved as binary (.BIN) files, which enabled the RGB pixie values to be extracted by MATLAB. At each condition, ten images of the flame were taken. These pictures were taken with a uniform time interval between each image (0.1 seconds). Three of the ten images were selected to be representative of the flame at each condition. These images were analyzed and the

temperature and emissivity results averaged to yield the results presented in this work. More details regarding the processing of the images with the MATLAB code are presented in the appendix.

The camera contained a standard 1/3" CCD panel with a resolution of 494 x 658 pixels. The camera is small (83x50x39 mm) and lightweight (200 g) and was mounted with a 25 mm focal length, c-mount lens. Although the lens has a continuous aperture, it was modified to enable 14 discrete aperture settings. To ensure a shallow focus, the aperture was allowed to remain completely open for all the data presented.

5 RESULTS – APPLICATION OF TWO-COLOR PYROMETRY TO COAL FLAMES

The following section presents both discussions and final results for various operating conditions. First, images and two-color pyrometry results are presented in a discussion regarding which emissivity model is more appropriate for this application. Next, an investigation in measurement interference from wall radiation and air entrainment is presented.

5.1 Determination of Proper Emissivity Model

An image of an oxy-coal flame with temperature and emissivity maps calculated using the Hottel and Broughton and gray emissivity models is shown in Figure 5-1. The image on the left is the original image obtained from the RGB camera containing all three colors. The image was obtained looking through an open port in the reactor and looking slightly upward (~30 degrees from the horizontal) at the root of the flame as it exited the burner. The coal and oxidizer are flowing from top to bottom in the image. The dark, uneven edges surrounding the flame are slag buildup around the port opening. At the time the image was taken, two pieces of slag were hanging from the burner block and are seen as black protrusions at the top of each image.

Although the flame is attached, light and dark streaks are seen primarily in the vertical flow direction. These streaks are caused by the uneven distribution of coal and the resulting uneven pockets of burning coal and volatiles. In the bottom, right corner of the RGB image, a speckled pattern is seen showing evidence of individual particles. A single pixel images an area approximately 500x500 μm, which is too large an area for an individual particle to be resolved.

The image provides an average emission from particle clouds which appear to be composed primarily of soot particles.
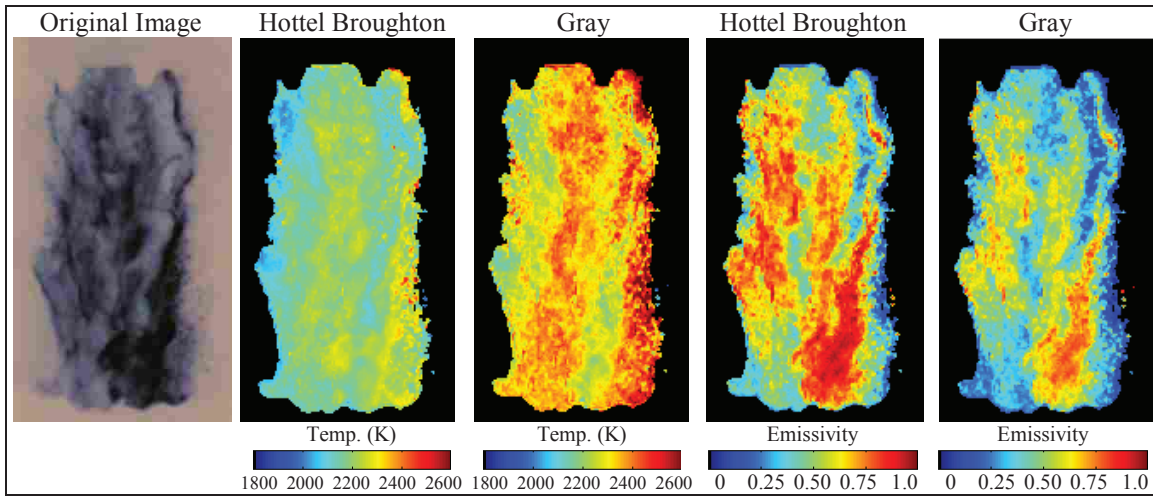
Figure 5-1. Left to right: original flame image, Hottel and Broughton temperature map, gray temperature map, Hottel and Broughton emissivity map, gray emissivity map.

To the right of the original image are maps of temperature and emissivity obtained using the two different emissivity models. Interestingly, the regions of highest luminosity in the original image are not the regions of highest temperature. Instead, the regions of highest luminosity correlate more closely with regions of higher emissivity. This result points out that visual observation and simple images of flames can be misleading with regard to temperature. Often the brightest parts of a flame are not at the highest temperature.

For the most part, the maps produced by the two different emissivity models produce images that have similar locations of high and low temperature and high and low emissivity, but the magnitudes are significantly different between using the two different emissivity models. In all cases, the Hottel Broughton temperatures are lower and the emissivities are higher than the gray model results.

Temperature distributions for each pixel in the flame using the two emissivity models are shown in Figure 5-2 and the average temperature and emissivity for both models are summarized

in Table 5-1. The Hottel and Broughton model produces a narrower temperature range (1940-2390 K) than the gray emissivity model (2100-2660 K). The average temperature obtained using a gray model was 2337 K, which was 154 K, or 7%, higher than the temperature obtained with the Hottel and Broughton emissivity model, 2183 K. The emissivity obtained with the gray model was 0.45 compared to 0.59 for the Hottel and Broughton model result. Thus, the gray model produced an emissivity 24% lower than the Hottel and Broughton model.

A) Hottel and Broughton

B) Gray
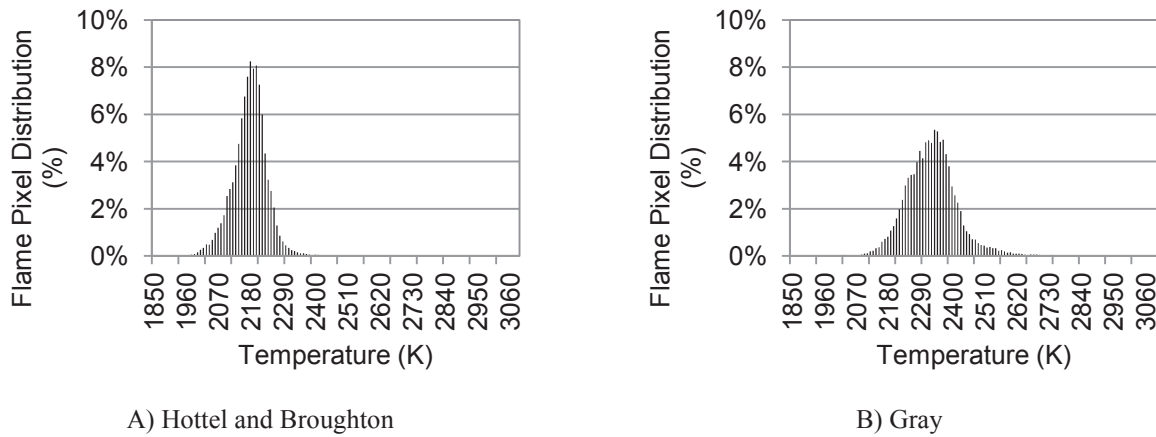
Figure 5-2. Temperature distribution of flame pixels calculated using A) the Hottel and Broughton emissivity model and B) the gray emissivity model.

Table 5-1. Measured average temperature, emissivity and the percent difference for the Hottel-Broughton and Gray emissivity models.

	Hottel and Broughton	Gray	Difference (%)
Temperature (K)	2183	2337	7.1
Emissivity	0.59	0.45	24.2

Because the difference in results produced by the two emissivity models is significant, it is important to determine which model is closer to the correct result. To do so, one must consider the images obtained and the processes involved in coal combustion. The images show that the coal flame is not confined to a single, narrow region separating fuel and oxidizer as occurs in a candle diffusion flame. Instead, the coal flame is an accumulation of numerous individual flame

structures which are formed by a combination of reacting volatiles within the turbulent flow field. Our conceptual model of a coal flame is therefore an accumulation of numerous flamelets grouped together to form a larger flame structure. Individual flamelet structures are clearly visible in the flame image as shown in Figure 5-1. The question arises as to whether the emission captured in the images from these flamelet structures is from soot or from burning char.

Fletcher et al. [26] discuss how soot is formed in clouds trailing behind individual coal particles. Soot produces the visible yellow emission as it burns in the flame surrounding these particles. Rather than the individual particles described by Fletcher et al [26], theses images show flamelets which surround pockets of coal particles. Soot burns as is passes through the thin reaction zone surrounding these pockets. Primary soot particles are very small (30 nm) and will follow even the very highest of turbulent flow accelerations. An image of soot should therefore appear as a bright thin layer wrinkled to match the turbulent structures of the flow. This appears consistent with a large portion of the flame image.

While soot is being oxidized in a flame zone surrounding coal, char and ash particles, emission from these particles must pass through the both the flame boundary and the soot in order to be observed by the camera. The time scales for volatile release and combustion including soot oxidation are much shorter than for the oxidation of char; therefore, the char emission, which is initially blocked by soot, should persist past the time of soot oxidation. Highly resolved images of the coal flame should be able to reveal groups of individual burning char particles. Evidence of this type of emission is seen in the individual color pixels at the bottom, right edge of the flame image and in some locations throughout the flame.

Evidence of both char and soot emission exists in the flame image. The majority of the image appears to contain turbulent reacting flow structures (flamelets) surrounded by thin sheets

of burning soot. However, evidence of individual burning particles is also seen. On the lower right boundary of the RGB image, numerous individual red, green and blue pixels can be identified. These pixels should contain emission for all three colors and yet they appear to be dominated by only one of the three. One explanation for these colors is that the camera is attempting to image a particle smaller than the resolution of a single pixel. The light is therefore focused on a fraction of the pixel, or one of the pixies that make up a single pixel. For example, if the light is focused on a green pixie, the image records green. Also, some of these pixels are separated from the flamelet structures indicating individual burning particles. These particles are probably some of the larger particles which require a longer burnout time.

Fletcher et al. [26] reports that 10-20% of the mass of a coal particle is converted to soot. Using the following assumptions, one can calculate the projected surface area of soot to that of a coal particle. Soot is assumed to be a 30 nm sphere with 1.8 g/cm^3 density and to be formed from 10% of the coal mass. The coal is assumed to be a 60 μm sphere with 1.34 g/cm^3 density. For this example, the projected surface area of soot is 40 times that of coal. Using Mie extinction theory [28] for spherical particle clouds, it can be calculated that 60 μm particles are 5 times more efficient at absorbing light than the smaller 30 nm particles. The net effect is that when soot is present, it can easily produce eight times the absorptivity (emissivity) of burning char. This combined with the fact that soot will burn at a higher temperature because it is a smaller particle, indicates that, when present, soot is the dominant emitter. It is therefore concluded that for the majority of the flame image, an emissivity model which takes into account the spectral nature of soot will be more accurate than a gray model. Thus, the Hottel and Broughton model was used to calculate all the results presented hereafter in this work. However, this does not mean that one emissivity model is correct for all locations in the flame. To be safe, one should consider the

uncertainty associated with the use of a single model to be on the order of 7% for temperature and 24% for emissivity.

Using the Hottel and Broughton emissivity model, images of temperature and emissivity for two operating conditions were processed and are shown in Figure 5-3. The results in the top row repeat the data shown in Figure 5-1. The operating conditions for both cases are summarized in Table 5-2; Case 1 has low CO_2 dilution and Case 2 has high CO_2 dilution produced by an increased flow in the secondary stream. The addition of CO_2 to the secondary flow, which doubles the ratio of secondary flow to total flow, also increases the mixing between fuel and oxidizer. This can be seen in the differences between the original images; the luminous regions in Case 2 are more distributed throughout the flame, while the dark regions in Case 1 are larger and more vertical. The higher mixing produces more uniform luminosity, temperature, and emissivity. Although the original images appear to be of similar luminosity, the combination of filters and exposure times is different for the two images, such that the gain on the bottom image is nine times that of the top image. The magnitude of luminosity is clearly much lower in the case with added CO_2. This is to be expected, because the CO_2 dilutes the mixture and reduces temperature. The added CO_2 is also expected to increase mixing, reduce fuel rich regions, and reduce the formation of soot.

Table 5-2. Operating conditions for Case 1 and 2.

Case	Coal (kg/hr)	Center O_2 (kg/hr)	Primary CO_2 (kg/hr)	Secondary O_2 (kg/hr)	Secondary CO_2 (kg/hr)	Oxygen Participation Ratio (% vol.)
1	18.00	21.4	25.00	21.4	0.00	70.14
2	18.00	21.4	25.00	21.4	40.00	47.46

The mean and maximum temperatures measured for each flame are compared to the adiabatic flame temperature in Table 5-3.

45
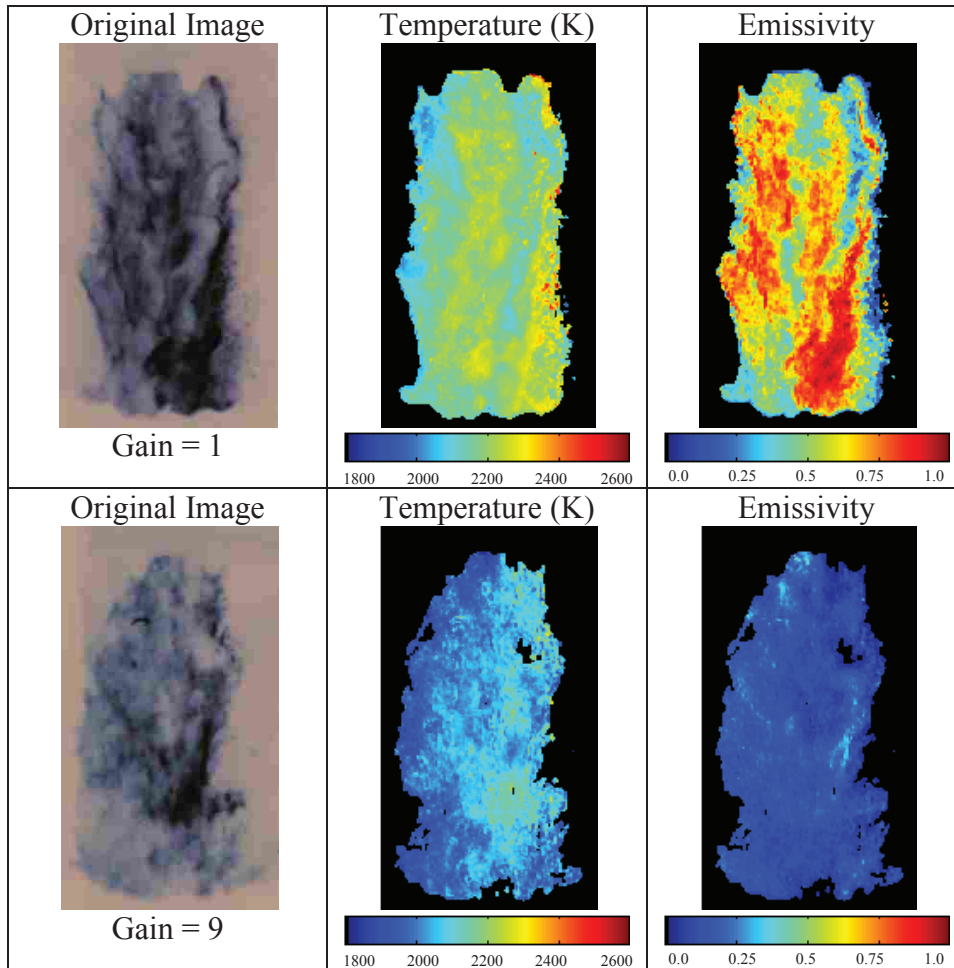
Figure 5-3. Top row from left to right: Case 1 original image, temperature map, emissivity map; Bottom row from left to right: Case 2 original image, temperature map, emissivity map.

The measured temperatures decrease with increasing CO_2, which follows the decreasing trend in the calculated adiabatic flame temperatures. The maximum temperatures measured in the flame are below the adiabatic flame temperature by 5.9% for Case 1 and 10.2% for Case 2. The two average temperatures are 25.3 and 23.2% below the Case 1 and 2 adiabatic flame temperatures respectively. This large difference is produced by the relatively large distribution of temperatures within the flame as shown by the distribution function in Figure 5-2. The reasons for this wide distribution and the relatively low average may the result of several factors. First, the emission from one flamelet may be partially absorbed along a line of sight by colder coal, char, ash, and

46

soot between the flamelet and the camera. A second reason is heat transfer from the soot to the water-cooled walls. Brown and Fletcher [27] report a decrease in flame temperature of 300 K by adding soot to a model of a reacting coal flame. Their conditions were for air-fired coal combustion. The high oxygen concentrations used in this work produced much higher flame temperatures and therefore the potential for greater heat loss.

Table 5-3. Summary of the measured mean, maximum and adiabatic flame temperature and mean measured emissivity for Case 1 and 2.

Case	Meas. Mean Temp. (K)	Meas. Maximum Temp. (K)	Adiabatic Flame Temp. (K)	Meas. Mean Emissivity
1	2183	2751	2925	0.59
2	2022	2365	2635	0.13

5.2   Uncertainty Analysis of Flame Temperature

Svensson et al. [17] characterized the uncertainty of the two-color method using the same equipment as this work to measure the temperature and emissivity of a diesel flame. The uncertainties included the inherent noise associated with the digital array. For a given pixel, a single emissivity and temperature in the two-dimensional array, the uncertainty of the emissivity was determined to be +/-20%, while the temperature had an uncertainty of +6% and -2%. In addition to these uncertainties, the accuracy of the measurement is dependent upon the operating conditions of the reactor.

This section investigates uncertainties involved with the collection method on the two-color temperature and emissivity results. Two specific operating procedures were examined: the effect of an unsteady wall temperature and the effect of the open port. The reactor walls contain a considerably large thermal mass that requires hours to reach steady state. Burner flow rates can reach steady state in a matter of minutes. The error in the flame temperature associated with a wall temperature that was not yet at steady state was quantified. All of the flame temperature

measurements were obtained with the reactor port removed to allow direct imaging of the flame. Removing the port door allows the entrainment of room air into the reactor and may impact the flame temperature. This error was also quantified. The operating conditions for the various cases used to investigate these effects are summarized in Table 5-4.

Table 5-4. Operating conditions for cases used to investigate the effect of transient wall temperature and air entrainment on measured flame temperature.

Case	Coal (kg/hr)	Center O_2 (kg/hr)	Primary CO_2 (kg/hr)	Secondary O_2 (kg/hr)	Secondary CO_2 (kg/hr)	Oxygen Participation Ratio (% vol.)
1	18.00	4.3	25.00	38.44	0.00	70.14
2	18.00	4.3	25.00	38.44	40.00	47.46
3	18.00	21.4	25.00	21.4	0.00	70.14
4	18.00	21.4	25.00	21.4	40.00	47.46

5.2.1   Transient Wall Temperature Interference

Figure 5-4 shows the wall temperature of the reactor, the measured flame temperature and the emissivity as a function of time. These data begin after the reactor was preheated with natural gas to a wall temperature of approximately 1200 K and end when the reactor walls reached a steady state temperature running at the Case 1 conditions in Table 5-4. The wall temperature was found by averaging the two thermocouple temperatures in the top two sections of the reactor (the sections where the flame is located).

The figure shows the wall temperature increased 275 K, or 23.8% above the initial temperature over a period of 1.7 hrs. During the same time period, the measured flame temperature increases by 75 K, or 3.4% of its initial temperature. The emissivity shows more scatter than the temperature and decreases from 0.30 to 0.27 (10%) over the same time period. These results are consistent with a decrease in heat loss from the flame due to the smaller temperature gradient. The temperature change observed in the walls is similar to that of the

largest change in steady state wall temperature for all of the operating conditions. Therefore the wall temperature does produce a modest impact on the measured flame temperature.
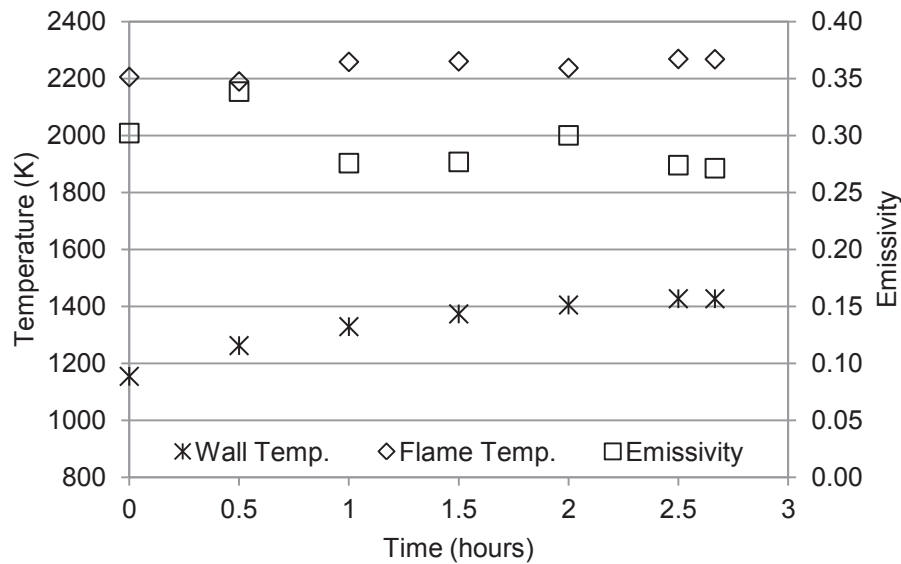
Figure 5-4. Wall temperature, flame temperature and emissivity as a function of time.

A second experiment was performed by rapidly changing the operating condition from Case 1 to Case 2 to reduce the flame temperature at constant wall temperature. The results are shown in Figure 5-5. The circled data points were taken operating at Case 2; all other data points were taken at Case 1 operating conditions. The flame temperature dropped 240 K from 2260 K to 2020 K or 10.6%. This result demonstrates that changes in the flame temperature due to changes in operating condition are larger than the change due to wall temperature; however, the change in flame temperature due to wall temperature is not insignificant.

Different flow rates of center oxygen and secondary CO_2 change the radiative heat transfer properties of the flame and thus change the reactor wall temperature if allowed to reach steady state. As achieving steady state takes hours, it was not practical to reach steady state in between each condition examined, even though that is probably essential to obtain the correct temperatures. Instead, the reactor was allowed to achieve steady state using the operating

conditions for Case 1. Thus, all the data were taken while the walls were in the range of this steady state temperature (~1400-1500 K). This maintained wall temperature consistency, but decreased the difference in flame temperature between other operating conditions. Cooler conditions will have temperature data skewed somewhat upward and hotter conditions will have temperature data skewed somewhat downward.
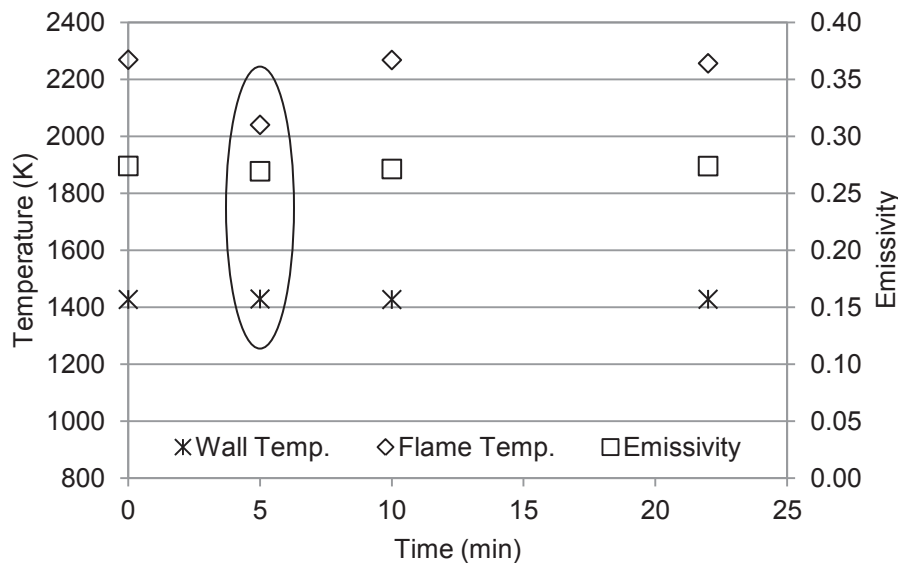
Figure 5-5. Wall temperature, measured flame temperature and emissivity as a function of time. The circled data were taken operating at Case 2; all other data were taken operating at Case 1.

5.2.2 Air Entrainment

To investigate the effects of air entrainment on temperature and emissivity, data were taken at four different operating conditions and at three different reactor pressures. These data are presented in Figure 5-6 and Figure 5-7. The four conditions were chosen at the different extremes of center oxygen and secondary CO_2 flow rates as shown in Cases 1-4 in Table 5-4 to ensure that the air entrainment at all extreme conditions was negligible. At each operating condition, the reactor pressure was changed from maximum negative to maximum positive. With the gate valve on the exhaust line closed, the fan pulled maximum flow through the reactor

creating a maximum negative pressure. This condition entrained more air into the reactor than was entrained during any of the experiments. With the gate valve open, room air was drawn into the fan instead of exhaust gas, producing a positive pressure in the reactor. This positive pressure caused product gas to exit the reactor through the open port into the room. Running the reactor with this high positive pressure was hazardous and could only be allowed for a brief period while collecting an image. A more neutral reactor pressure between these two extremes was also investigated.

Results for the open reactor port experiments are shown in Figures 5-6 and 5-7. The temperature data for the three reactor pressures at each case are close together, with an average standard deviation of 14 K (0.7% of the average measured temperature) with a maximum standard deviation of 29 K (1.3% of the average measured temperature at that case). As variation within this magnitude is expected for the temperature measurement, it is concluded that the temperature is not affected by air entrainment into the reactor. The emissivity data are more scattered. The data at each case have an average standard deviation of 0.0206 (7.6% of the average emissivity) with a maximum standard deviation of 0.0331 (12.2% of the average emissivity at that case). It is expected that the emissivity data are more scattered, since emissivity is a more prone to be affected by noise in the system. No trend in the temperature or emissivity results as a function of the changing pressure can be seen. For example, neither the temperature nor emissivity is always higher when the reactor pressure is positive. This proves that the temperature and emissivity data are not influenced by changing the reactor pressure and the entrainment of air. In fact, the average standard deviation between the three representative images taken at each condition was higher (24 K and 0.024) than the average standard deviation between the three pressures at each operating condition (14 K and 0.0206). Therefore, all further

51

data presented were taken at a neutral reactor pressure, which had a slight risk of air entrainment, rather than the positive reactor pressure, which had no air entrainment but presented safety concerns.
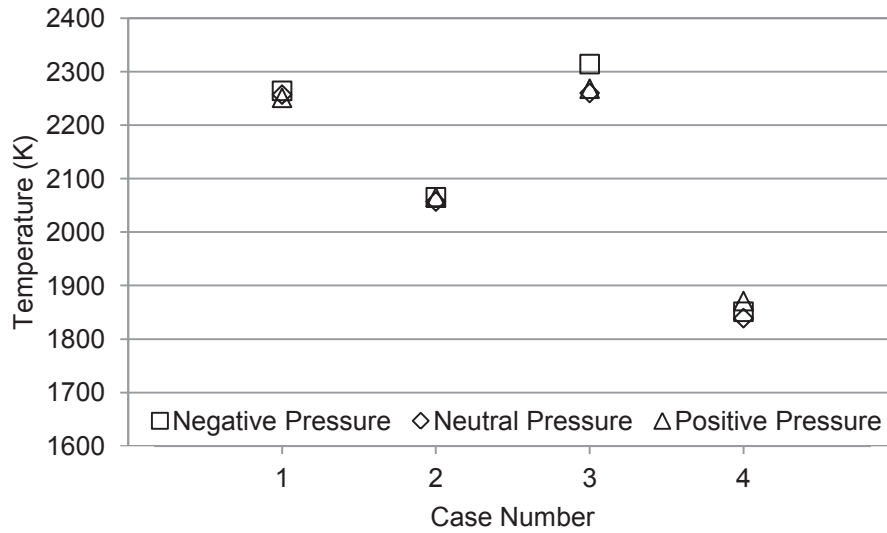

Figure 5-6. Temperature taken at four different conditions with negative, neutral and positive reactor pressures.
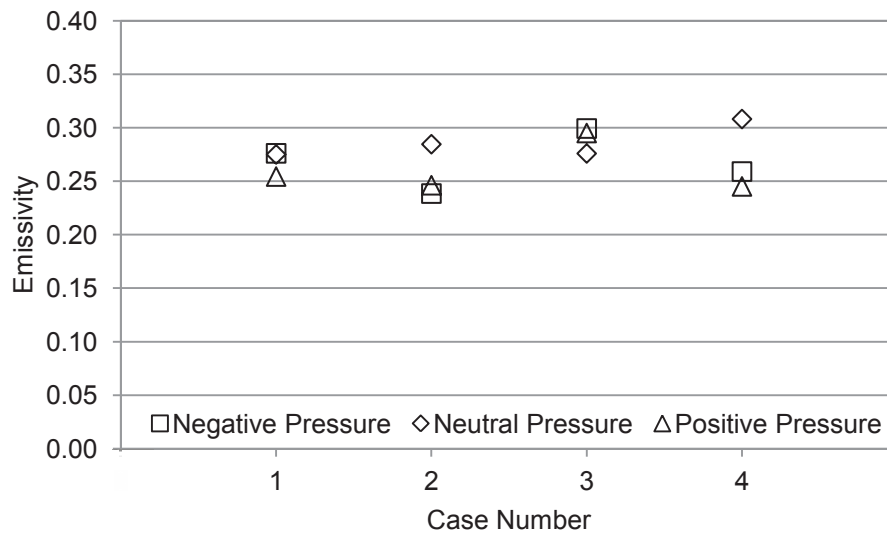
Figure 5-7. Emissivity taken at four different conditions with negative, neutral and positive reactor pressures.

5.2.3 Summary

Based on the results presented in this chapter, it was concluded that temperature and emissivity data would be taken using the Hottel and Broughton model. The collection of imaged flame data could be taken with the reactor port open and a neutral reactor pressure without adversely impacting the flame temperature. Reactor wall temperatures were found to alter the flame temperature. The maximum impact of wall temperature on flame temperature is on the order of 75 K. Because the time required to reach steady state is on the order of hours, the wall temperature was heated to ~1400-1500 K before collecting data. Wall temperatures were recorded and data were taken rapidly at a constant wall temperature. Thus, the variations in measured flame temperature between conditions will be under-predicted at hotter conditions and over-predicted at cooler conditions by no more than 75 K.

6   RESULTS – FLAME TEMPERATURE AND EMISSIVITY FOR THREE SWIRL ANGLES

After demonstrating the use of two-color, digital pyrometry on a pulverized-coal flame, the technique was used to investigate the performance of an oxy-coal burner with three different swirl vanes, oxygen split between two burner streams and variations in CO_2 flow rate. The operating conditions studied are shown in Table 1-1. Representative images of the flames will be shown followed by the lift-off length, average temperature, and average band emissivity of each flame.

For each operating condition, a set of images was collected. After visually inspecting these images, three images that were representative of the group were selected for detailed analysis. This analysis included identifying the flame pixels and then calculating the temperature and visible band emissivity at each flame pixel. Once the temperature and emissivity at each pixel were known, the results for each pixel were averaged to produce an average temperature and emissivity for each image. The average results for the three representative images were averaged to provide the average temperature and emissivity data at each condition. If the flame was not already formed at the burner exit, the lift-off length between the flame and the burner was also calculated. The lift-off length was defined as the distance from the burner exit to the first row of pixels where flame data existed for more than half of the image width. Finally, axial temperature and emissivity profiles are presented for each swirl vane. The axial profiles were obtained by averaging rows of pixels at various axial distances from the burner.

6.1   **No Swirl Vane Temperature and Emissivity Results**

Table 6-1 is a matrix of representative flame images as a function of center oxygen (O_2-C) and secondary CO_2 (CO_2-S) flow rates for the burner with no swirl vane. Only images up to 20 kg/hr CO_2-S are shown, because the flame became too unstable above 20 kg/hr CO_2-S to maintain operation. For the other two swirl vanes, conditions of up to 40 kg/hr CO_2-S are presented. Each picture is labeled with its associated gain to enable luminosity comparisons between the settings. The top row of images contains conditions with no secondary CO_2 flow rate with increasing center oxygen flow rates from left to right. The first few images were taken with the same gain, 2.0, which is twice the baseline gain of the brightest images presented in this work. The brightest images were taken when running with the 15° swirl vane. The gain increases with center oxygen and secondary CO_2 flow rates, meaning that the flames decreased in visible intensity as these flow rates increased. On the bottom row, the gain is the lowest for the 8.5 kg/hr O_2-C image and higher on either side, indicating that at 20 kg/hr CO_2-S, the brightest flames were produced at this center oxygen flow rate.

Several observations can be made from these images. The flames are seen to be detached on the left columns of images (low O_2-C) and are the most detached on the bottom row (high CO_2-S). Thus, the lift-off length is seen to increase with decreasing center oxygen and increasing secondary CO_2 flow rates. Generally, the visible intensity seen in the images is highest at between 8.5 and 12.8 kg/hr O_2-C and decreases at lower and higher center oxygen flow rates. The final observation is more subtle. The flames on the bottom and to the right (conditions with higher incoming flow rates, thus higher incoming velocities) have finer turbulent structures than flames to the left and on the top (conditions with lower incoming gas velocities). These finer structures indicate increased turbulent mixing. At low gas velocity conditions, the flames have a

defined, sheet-like quality with areas of differing intensities. At high gas velocity conditions, the flames look more evenly distributed in intensity, fuzzier and more out of focus. These images required a higher gain, which lengthened the exposure times. These longer exposure times contribute to the fuzzier, out of focus look of the images.

In order to better quantify the impact of flow parameters on the lift-off length of the flame, the lift-off lengths using no swirl vane are shown in Figure 6-1. To determine the lift-off length, the flame boundary was defined using a MATLAB-based, edge-finding algorithm. The lift-off length was defined to be the distance from the burner base to the row where half the pixels in that row were contained in the flame boundary.

Table 6-1. Matrix of representative flame images for no swirl vane. Rows contain conditions at various secondary CO_2 flow rates; columns contain conditions at various center O_2 flow rates. Image gains are labeled above each image.
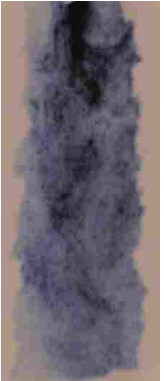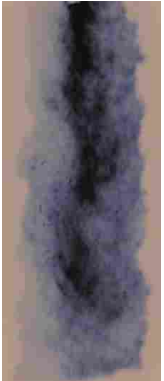
	1.7 kg/hr O_2-C	4.3 kg/hr O_2-C	8.5 kg/hr O_2-C	12.8 kg/hr O_2-C	17.1 kg/hr O_2-C	21.4 kg/hr O_2-C
0 kg/hr CO_2-S	GAIN=2.0	GAIN=2.0	GAIN=2.0	GAIN=2.0	GAIN=3.1	GAIN=4.2
10 kg/hr CO_2-S	GAIN=3.1	GAIN=2	GAIN=2	GAIN=2	GAIN=4.2	GAIN=6.3

Table 6-1 Continued

| | GAIN=4.2 | GAIN=4.2 | GAIN=3.1 | GAIN=4.2 | GAIN=5.2 | GAIN=10.4 |
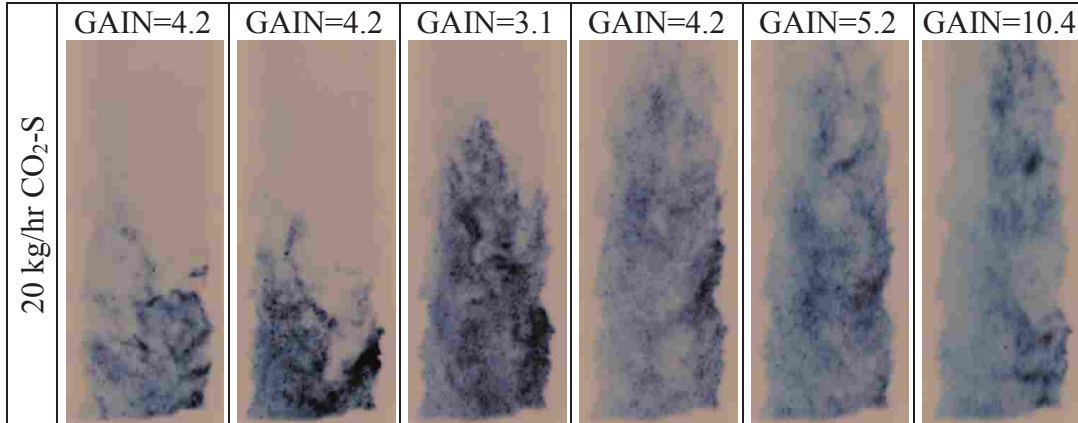
The three representative images for each condition were analyzed to determine lift-off length and the results for the three images were averaged. It should be realized that the pixel intensity from one image to the next is relative to the exposure time and aperture setting of the camera. Therefore, the lift-off lengths presented are not a precise measurement but rather an estimate of the onset of chemical reaction. Figure 6-1 quantifies the trends seen in Table 6-1, namely, that the lift-off length decreases with increasing center oxygen and secondary CO_2 flow rates.
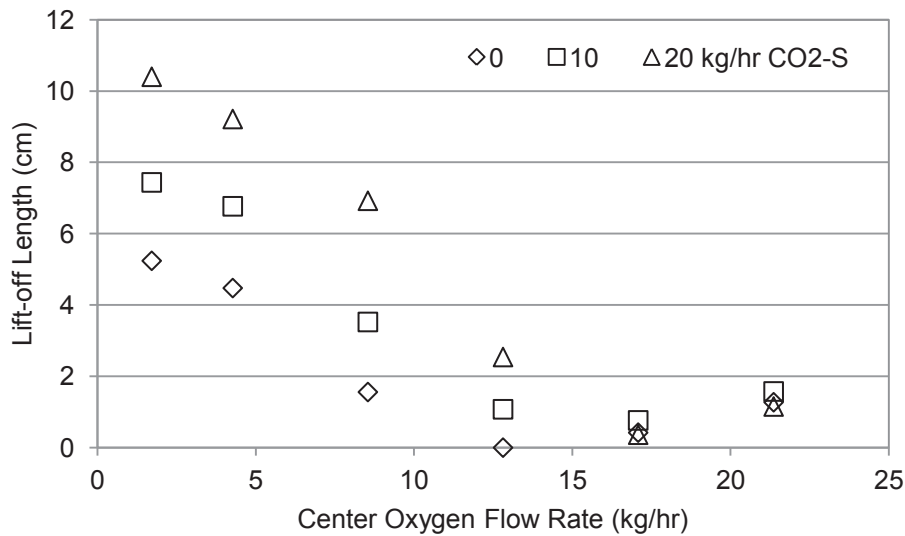
Figure 6-1. Lift-off length as a function of center oxygen flow rate for each secondary CO_2 flow rate using the no swirl vane.

Figure 6-1 also shows that at high center oxygen flow rates, the lift-off length increases slightly. As can be seen in Table 6-1, this is not true. This slight increase presented in lift-off length is due to an inherent flaw in defining where the flame begins. At high center oxygen flow rates, the velocity through the center tube was quite large due to its small diameter, which caused the flame to thin. Thus, the pixels defined in the flame boundary were not more than half of the row at the burner exit. This caused a false lift-off length to be reported for those conditions.

The energy required to heat and ignite the incoming fuel stream can be provided by radiation from the surrounding walls, mixing with product gas (hot recirculated products), or thermal diffusion upstream from the flame. Normally, coal flames are stabilized predominantly by mixing hot, recirculated, product gas with incoming, ambient temperature coal and oxidizer. This mixing of these hot product gases with the incoming streams is caused primarily by swirling one or more of the incoming streams, which creates a negative pressure below the center of the burner. This negative pressure causes the product gases to flow back up through the center of the flame toward its root where the incoming fuel and oxidizer streams are exiting the burner. This is illustrated in Figure 6-2, which presents a cross section of a simple burner at the exit. The flow through the swirled fuel and primary CO_2 stream is depicted by the helical line beginning in the burner that widens after it exits. The red line symbolizes the flame boundary. The straight lines coming from the annulus on either side of the fuel and primary CO_2 stream represent the flow lines of the unswirled secondary stream. The rounded vectors within the flame boundary represent the recirculation path of hot product gases. If there is a greater amount of swirl given to the incoming gases, there is a greater amount of product recirculation. This experimental burner has a relatively low swirl number even when using the highest swirl vane (always less than 0.15). The only swirled stream is the coal and primary CO_2 stream, which has a lower flow rate and

smaller radius than the unswirled secondary flow. This lack of recirculation produces the potential for lifted flames. The flames presented in this section, which have no swirl added, had such a large amount of lift-off that conditions above 20 kg/hr secondary CO_2 could not be taken. After that point, the lift-off length became too great and the flame became dangerously unstable.
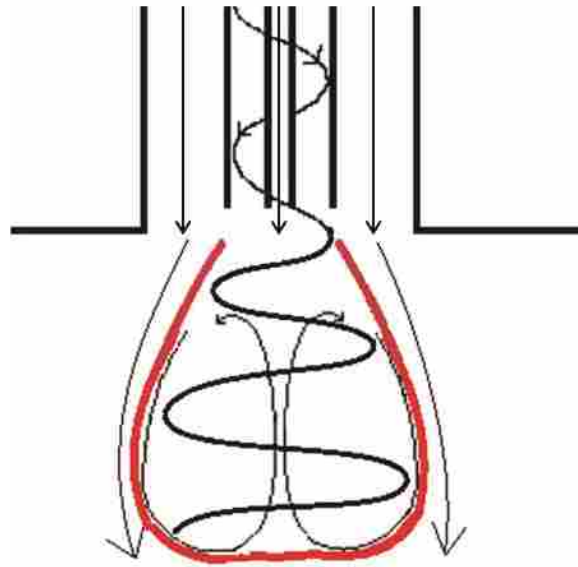
Figure 6-2. Illustration of burner flow patterns with swirl added to the fuel stream.

Since the introduction of center oxygen cannot be argued to increase heat transfer to the incoming fuel by radiation, mixing, or diffusion, it is most likely that increasing center oxygen decreases the temperature, or energy, required to produce ignition. That is why a decrease in lift-off length is seen as center oxygen flow rates increase. On the other hand, increasing the secondary CO_2 flow rate adds additional, cold, inert gas to the secondary stream. This addition results in a higher heat capacity of the secondary stream, which means more energy is required to heat the fuel and oxidizer to the ignition temperature. Therefore, the addition of secondary CO_2 delays ignition and increases lift-off length.

The visible luminosity of the flame is a function of both its temperature and emissivity. A flame that is brighter than another may be at a cooler temperature if its emissivity is higher.

Thus, conclusions about the relative temperature of the flames cannot be made without analyzing the images for temperature and emissivity.

In order to understand the temperature and emissivity trends, it is important to consider a physical model of coal combustion and the coal flame. A diagram showing steps in a proposed pulverized coal combustion process is shown in Figure 6-3. Coal enters the combustion chamber entrained in CO_2. The coal and primary CO_2 mixture is mixed with oxidizer from the center and secondary streams and hot combustion products, which are primarily CO_2 and H_2O in oxy-combustion. The coal and primary CO_2 receive energy through radiation from the hot reactor walls and from mixing with the hot products (Step 1). The increase in temperature of the coal releases volatiles from the coal, which form a gaseous mixture surrounding the coal particles (Step 2). The volatiles in the mixture ignite and burn rapidly, producing additional hot products. This mixture may continue to be fed by additional volatile release from the coal as it continues to be heated. This mixture is typically fuel rich with insufficient oxygen to complete combustion, as described in Figure 6-3, but the stoichiometric ratio of the mixture is dependent on the amount of mixing that occurs prior to ignition (Step 1). If fuel rich, a flame forms around the hot products at the location where the fuel rich mixture and surrounding oxidizer are near stoichiometric. This fuel rich mixture surrounded by flame is a coal flamelet (Step 3). The flamelet may be large in size (similar in scale to the burner) or it may be as small as a single coal particle surrounded by a flame. Its size will depend on how soon ignition occurs relative to mixing and how dense the coal is distributed in the incoming carrier gas. Coal flamelets can take on various shapes depending on the fluid dynamics of the burner, including streaky, cylindrical tubes, thin sheets, fat sheets, and irregular spheres.
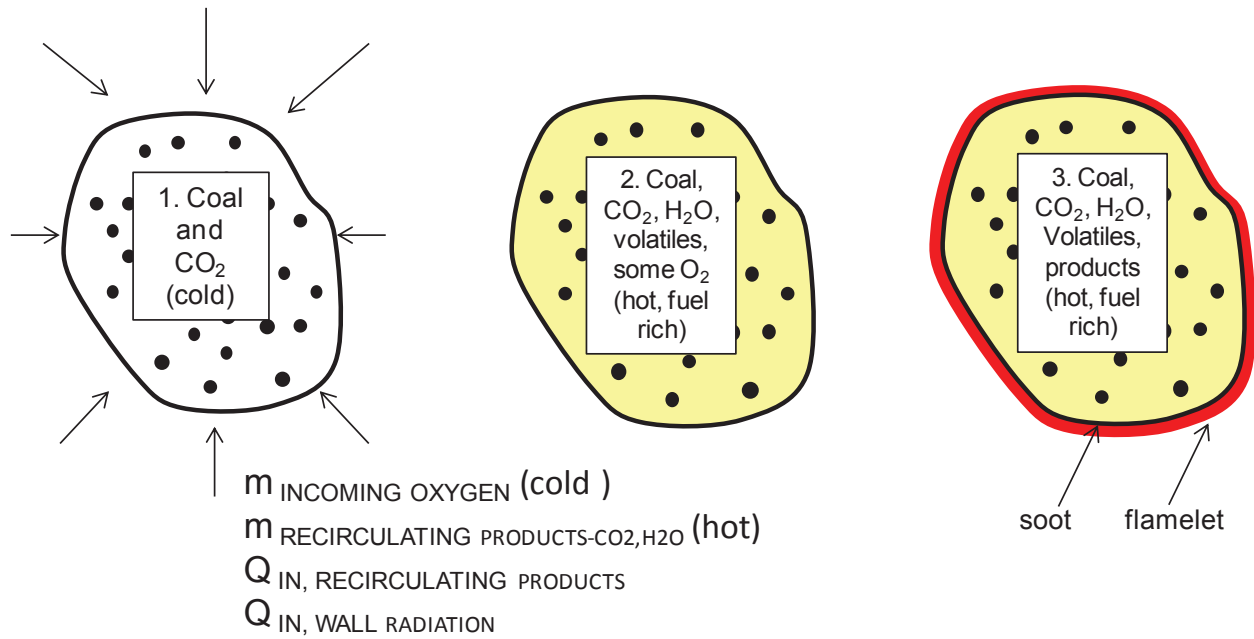
Figure 6-3. Illustration of the pulverized coal combustion process.

Soot particles are formed as heavy hydrocarbons in the volatiles agglomerate. These particles burn as they pass through the flamelet. Since the particles are small (20-40 nm), they reach within 1 K of the flame temperature [8] as they pass through it. Thus, imaging the radiation from these solid particles provides the temperature of the flame. The temperature at the flamelet boundary is produced by the reaction of fuel and oxidizer as illustrated by Equation (6-1). The fuel and oxidizer streams enter the reactor at a cold temperature (T_C) and the recirculated products are at a hot temperature (T_H). If there is no heat loss to the surroundings, then the reaction of the coal will form products at the adiabatic flame temperature (T_{Ad}). The adiabatic flame temperature can be reduced in two ways. First, diluents such as the CO_2 in the secondary stream introduce mass that must be heated from ambient (T_C) to product temperatures (T_{Ad}) but that does not participate in the reaction. Therefore, additional CO_2 absorbs more of the fuel energy released and lowers the adiabatic flame temperature. This is consistent with all the temperature data presented in this work. Second, additional diluents are introduced by the

product gas which is primarily CO_2 and H_2O. These products have lost heat before they participate in the flame reaction in Equation (6-1), so even though they are still hot (T_H), they are not as hot as the adiabatic flame temperature and will decrease it. The flame temperature is not actually at the adiabatic flame temperature, because there is heat loss to the surroundings. Thus, an addition way to lower the flame temperature is to increase the heat transfer from the flame. The bulk of the heat loss is radiation from either the reactants or products of the flame, but primarily from the soot. In summary, the measured flame temperature will be lower if the adiabatic flame temperature is lowered by adding additional diluent or increasing recirculation mixing, or by increasing the heat loss from the flame.

$$\text{Fuel}(T_C) + [O_2 + CO_2](T_C) + [CO_2 + H_2O](T_H) => [CO_2 + H_2O](T_{Ad}) \tag{6-1}$$

Figure 6-4 presents the spatially-averaged temperature results as a function of center oxygen flow rate for each secondary CO_2 flow rate using no swirl vane. The data show a clear trend of decreasing temperature with increasing secondary CO_2. The temperature reaches a maximum between 8.5 and 12.8 kg/hr center oxygen. The temperature decreases more significantly at higher center oxygen flow rates than it increases at lower center oxygen flow rates. The temperature decreases at high secondary CO_2 flow rates; however, the effect of secondary CO_2 on the flame temperature is smaller than the impact of changing the oxygen location.

The data show the expected decrease in measured flame temperature when CO_2 is added to the secondary stream and when parameters are changed which increase the mixing of products into the flame. Initial increases in center oxygen provide O_2 directly into the primary coal flow, which decreases the ignition temperature and shortens the flame lift-off length. The smaller lift-off length means that less diluent (CO_2 and H_2O) is mixed into the fuel jet, which causes the

temperature to increase. As center oxygen flow rates increase, the flame becomes fully attached and diluent entrainment due to lift-off is minimized. Further increases in center oxygen create a high velocity, low pressure jet, which lowers the temperature. This jet entrains diluent from the surrounding area, which decreases the temperature. Another possibility is that the jet also thins and lengthens the flame, giving it a greater surface area. This larger surface area could increase the heat loss from the flame and decrease the temperature.
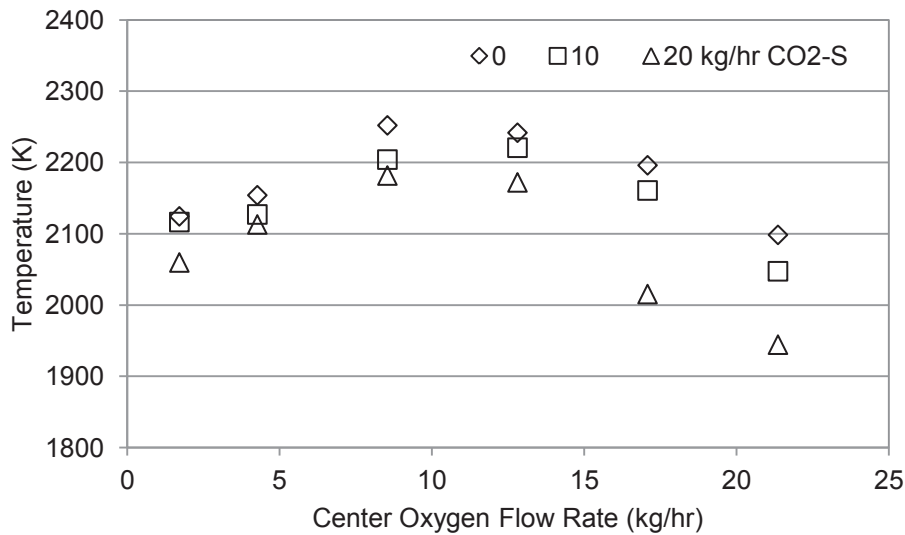

Figure 6-4. Temperature as a function of center oxygen flow rate for each secondary CO$_2$ flow rate using no swirl vane.

The temperature series at 0 kg/hr CO$_2$-S decreases from 2252 K to 2098 K (154 K) when moving from 8.5 to 21.4 kg/hr O$_2$-C, while the series at 20 kg/hr CO$_2$-S decreases from 2182 K to 1944 K (238 K) when moving between the same two conditions (from 8.5 to 21.4 kg/hr O$_2$-C). Thus, the series at 20 kg/hr CO$_2$-S has a much larger decrease in temperature than the series at 0 kg/hr CO$_2$-S when moving between the same two conditions. The smaller change for the 0 kg/hr CO$_2$-S series occurs because there is no cold, incoming diluent (CO$_2$-S) to entrain into the flame as the center oxygen jet forms. Thus, it seems that this decrease is mainly caused by entraining hot product gases and potentially from the increased heat transfer from the lengthened flame. It

63

appears the larger decrease at 20 kg/hr CO_2-S occurs not only because of the entrainment of hot product gas and the possible increased heat transfer from a lengthened flame, but also because a significant amount of the gas entrained into the flame is the cold CO_2 from the secondary stream.

Figure 6-5 presents the spatially-averaged emissivity results as a function of center oxygen flow rate for each secondary CO_2 flow rate using no swirl vane. The emissivity is thought to be dominated by soot particle radiation but may also be influenced by radiating coal particles. Typically, a higher emissivity is assumed to mean a greater concentration of soot particles. The emissivity does not vary widely with center oxygen flow rate. Emissivity increases from an average of 0.23 over all CO_2-S flow rates at 1.7 kg/hr O_2-C to a maximum average of 0.27 at 4.3 kg/hr O_2-C. The emissivity then decreases to an average of 0.12 at 21.4 kg/hr O_2-C. The emissivity data have a similar profile as a function of center oxygen as the temperature data, except that the maximum is shifted to a lower center oxygen flow rate and the emissivity at high center oxygen conditions approaches a constant value of 0.12. Emissivity tends to be highest for low secondary CO_2 flow rates and generally decreases with increasing secondary CO_2.

The differences in emissivity can be explained by changes in soot formation. Since soot is formed in the fuel rich regions within a flamelet and lifted flames have increased oxidizer entrainment, lifted flames should produce less soot and emissivity. This appears to be the case for flames with low center oxygen flow rates, which can be seen in the left column of Table 6-1 and are to the left in Figure 6-5. As more center oxygen is added, the lift-off decreases and the flame attaches (see Table 6-1) and soot concentration and emissivity increase. Soot and emissivity reach a maximum where the flame begins to attach (4.3 kg/hr O_2-C). A further increase of center oxygen provides even more oxygen to the fuel stream than entraining oxygen from the flame lift-off, inhibiting soot formation. Thus, adding center oxygen beyond 4.3 kg/hr

decreases soot formation and the emissivity. The decrease in emissivity at center oxygen flow rates below 12.8 kg/hr when secondary CO_2 is increased can be explained by the increased dilution and mixing that occur due to the higher velocity of the secondary stream, both of which inhibit soot formation.

The effect of oxidizer entrainment on soot formation is more significant when there is no CO_2, or 100% O_2, in the secondary stream than at the maximum secondary CO_2 setting, 20 kg/hr. This is illustrated when comparing the 0 and 20 kg/hr CO_2-S flow rates at low center oxygen flow rates. The emissivity at 20 kg/hr CO_2-S barely increases, while the series at 0 kg/hr CO_2-S has a significant jump, even though the initial addition of center oxygen decreases the lift-off length of the flame for both CO_2-S series. At the high secondary CO_2-S series, the flame was not entraining as much oxygen as at low CO_2-S, since the bulk of the secondary stream was CO_2. Thus, decreasing the lift-off length of the flame and reducing the amount of entrainment did not increase the soot formation much.
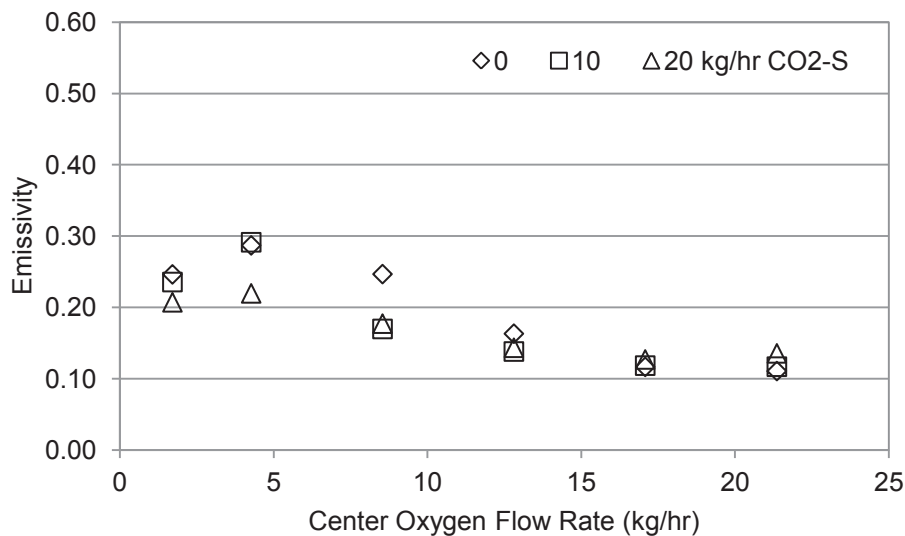

Figure 6-5. Emissivity as a function of center oxygen flow rate for each secondary CO_2 flow rate using the no swirl vane.

65

The adiabatic flame temperature as a function of the secondary CO_2 flow rates is shown in Figure 6-6. The adiabatic flame temperature does not change as a function of center oxygen flow rate, since the total amount of oxygen exiting the burner remains the same. The temperature is seen to drop 130 K as it goes from 2925 K at 0 kg/hr CO_2-S to 2765 K at 20 kg/hr CO_2-S. A fairly similar decrease in the measured temperature is expected, but the magnitude of the decrease may not follow the change in the adiabatic flame temperatures exactly, since the effects of adding CO_2 to the flame are complex. The measured temperatures averaged over all the center oxygen conditions dropped about 100 K when changing from 0 to 20 kg/hr CO_2-S. The temperature drop due to CO_2 addition is fairly close to the adiabatic flame temperature drop caused by adding CO_2, although the adiabatic flame temperatures are considerably higher than those measured.
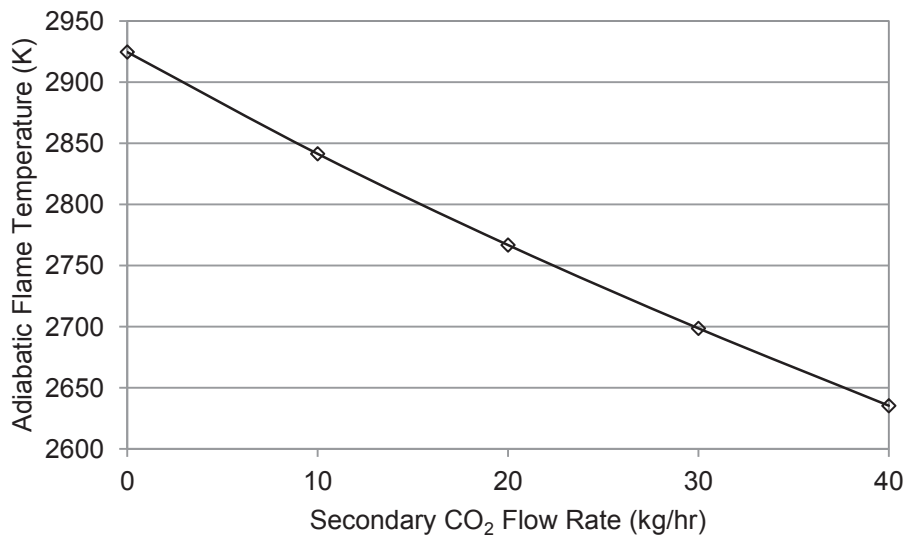

Figure 6-6. Adiabatic flame temperature as a function of secondary CO_2 flow rate.

The actual, measured flame temperatures are colder than the adiabatic flame temperature because of heat transfer from the flame, primarily from the soot, to the reactor walls. The total heat loss in the BFR has been measured by a heat balance with the cooling water for the reactor. The heat

loss to the walls is estimated to be on the order of 25-30%. This is on the order of the heat loss needed to drop the adiabatic flame temperatures to their corresponding measured average temperatures.

6.2   15° Swirl Vane Temperature and Emissivity Results

Table 6-2 is a matrix of representative flame images as a function of center oxygen and secondary CO_2 flow rates for the 15° swirl vane. It should be noted that due to the increased stability of the flame added by the swirl vane, images with conditions up to 40 kg/hr CO_2-S are presented. The first row of images, those at 0 kg/hr secondary CO_2, are the brightest presented in this work. They were all taken at the same gain, which is the baseline gain of 1.0. Similar to the images presented when using no swirl vane (Table 6-1), the flames on the bottom and to the right (high incoming velocities) have finer turbulent structures than flames to the left and on the top (low incoming gas velocities). These finer structures indicate increased turbulent mixing.

Table 6-2. Matrix of representative flame images for 15° swirl vane. Rows contain conditions at various secondary CO_2 flow rates; columns contain conditions at various center O_2 flow rates. Image gains are labeled above each image.
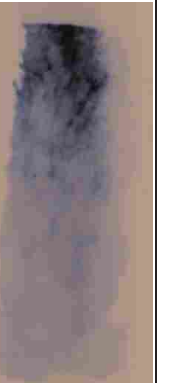
	1.7 kg/hr O_2-C	4.3 kg/hr O_2-C	8.5 kg/hr O_2-C	12.8 kg/hr O_2-C	17.1 kg/hr O_2-C	21.4 kg/hr O_2-C
0 kg/hr CO_2-S	GAIN=1.0	GAIN=1.0	GAIN=1.0	GAIN=1.0	GAIN=1.0	GAIN=1.0

Table 6-2 Continued

	GAIN=2.0	GAIN=2.0	GAIN=2.0	GAIN=2.0	GAIN=2.0	GAIN=4.2
20 kg/hr CO_2-S						
	GAIN=4.2	GAIN=4.2	GAIN=3.1	GAIN=4.2	GAIN=6.3	GAIN=10.4
40 kg/hr CO_2-S						

Figure 6-7 presents the lift-off length as a function of center oxygen for the images in Table 6-2. Similar to the results when using no swirl vane in Figure 6-1, the lift-off length generally increases with increasing secondary CO_2 and decreasing center oxygen flow rates. These trends are explained by the same reasons as discussed when using no swirl vane. The lift-off length at 21.4 kg/hr O_2-C and 40 kg/hr CO_2-S does not agree with the trends seen in all the other data. The corresponding image in Table 6-2 shows this flame is actually attached but a dark streak runs through the top, middle portion of the flame causing the algorithm to define the flame as lifted. This streak is thought to be caused by cold coal particles entering the reactor and getting swept directly into the high velocity oxygen jet without igniting. The flame does not fill over half of the total width of the open port until 3 cm from the burner exit. The magnitude of

lift-off length using the 15° swirl vane is smaller than that when using no swirl vane, even when the secondary CO_2 flow rate is doubled at the 15° swirl setting. This reduction in lift-off length is caused by adding swirl to the fuel stream. As explained previously, the addition of swirl causes a recirculation zone where hot product gases mix with incoming reactants and stabilize the flame, preventing lift-off.
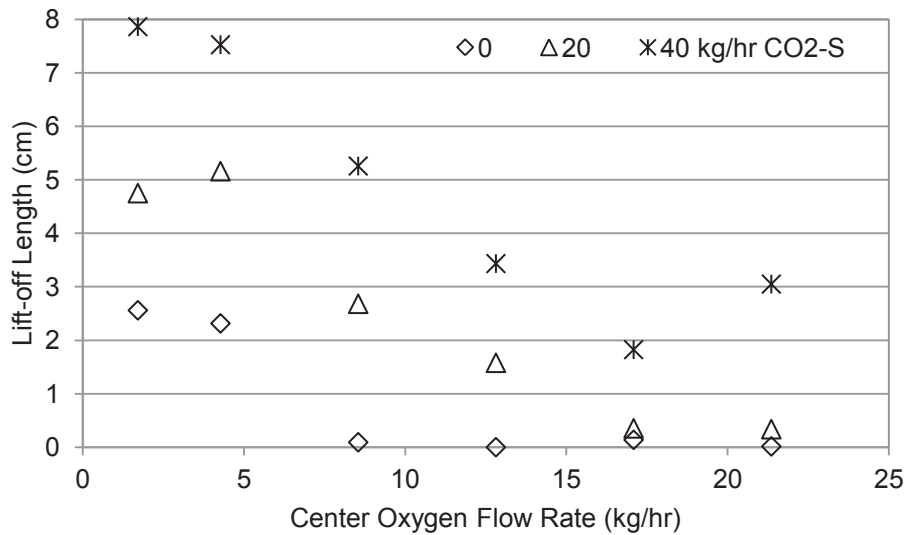

Figure 6-7. Lift-off length as a function of center oxygen flow rate for selected secondary CO_2 flow rates using the 15° swirl vane.

Figure 6-8 presents the spatially-averaged temperature results as a function of center oxygen flow rate for each secondary CO_2 flow rate using the 15° swirl vane. The data show a clear trend of decreasing temperature with increasing secondary CO_2. This is consistent with the cold CO_2 acting as a diluent to decrease flame temperature.

The data show a more complex relationship between center oxygen flow rate and the corresponding temperature. Interestingly, each series of constant CO_2-S fit very well with a fourth-order polynomial as seen in the Figure 6-8, which reveals a repeatable pattern in the data. Each CO_2-S series of data exhibit a minimum at low center oxygen flow rates and a maximum at high center oxygen flow rates. The maxima shift to higher center oxygen flow rates with

increasing secondary CO_2 flow rates. The repeatability of the trend seen for each CO_2-S flow rate suggests the data are correct and the trends are real.
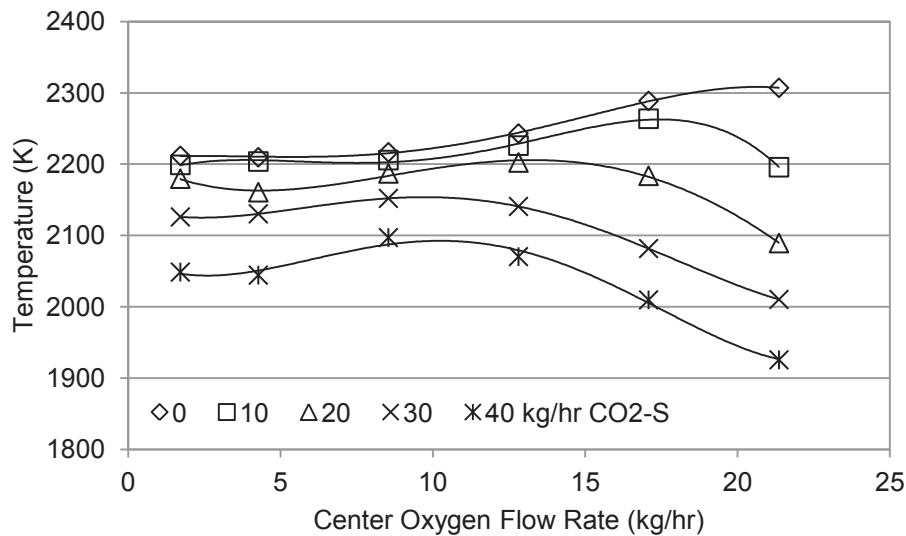

Figure 6-8. Temperature as a function of center oxygen flow rate for each secondary CO_2 flow rate using the 15° swirl vane.

While it is not possible to positively explain these complex temperature results, the location of the maxima shifting to higher center oxygen flow rates at lower CO_2-S flow rates is consistent with the lift-off length, which follows the same trend (Figure 6-7). It takes more center oxygen to attach a flame at high secondary CO_2 flow rates. This suggests that the increase in temperature producing the maxima is caused by reduced entrainment and shorter lift-off lengths. With less entrainment, there is less dilution from added CO_2 and recirculated product gas. Thus, the temperature is maximized when the center oxygen jet has minimized diluent entrainment. The drop in temperature at high center oxygen flow rates suggest that the high velocity jet of the center oxygen is causing increased mixing with the secondary stream and increased dilution. This increased dilution makes less difference when the secondary stream is pure oxygen and therefore, the 0 kg/hr CO_2-S stream does not decrease in temperature at high center oxygen flow rates. This change in maxima for the different CO_2-S settings was not seen at the 0° swirl vane.

70

This is most likely because the lack of swirl decreased the amount of entrainment from the diluted secondary stream.

Figure 6-9 presents the spatially-averaged emissivity results as a function of center oxygen flow rate for each secondary CO_2 flow rate using the 15° swirl vane. Like the data when using no swirl vane, the emissivity does not vary widely with center oxygen flow rate. It increases from an average of 0.25 over all CO_2-S flow rates at 1.7 kg/hr O_2-C to a maximum of 0.28 at 4.3 kg/hr O_2-C. The emissivity then decreases to an average of 0.17 at 21.4 kg/hr O_2-C. It again tends to be highest for low secondary CO_2 flow rates and generally decreases with increasing secondary CO_2. The emissivity for a fixed CO_2-S flow rate generally produces a maximum at intermediate center O_2 flow rates. This trend is similar to the 0° swirl results, except the emissivities continue to decrease at higher center oxygen flow rates and do not asymptote to a fixed value with increasing center O_2.

Adding center oxygen initially decreases entrainment by reducing ignition delay and attaching the flame but, once attached, the addition of center oxygen increases entrainment because of the high velocity jet produced by the center oxygen. The emissivities with the 15° swirl are higher at low center oxygen flow rate than the emissivities produced when using no swirl vane. This is thought to be caused by the swirl vane, which produced a fuel rich, recirculation zone, which creates more soot. Increasing center oxygen burns out the soot more effectively at low secondary CO_2 flow rates. At 0 kg/hr CO_2-S, the emissivity falls from 0.33 to 0.22 when moving from 12.8 to 21.4 kg/hr O_2-C. At 40 kg/hr CO_2-S, the emissivity falls from 0.20 to 0.18 when moving from 12.8 to 21.4 kg/hr O_2-C, a much smaller drop. At 0 kg/hr CO_2-S, the secondary stream only contains oxygen. Thus, increasing the center jet, which increases the entrainment of the pure oxygen secondary stream, will decrease the amount of soot in the flame.

At 40 kg/hr CO_2-S, the soot formation is already limited by the high concentration of CO_2 and increasing the center oxygen flow rate does not have as great an effect on soot formation.
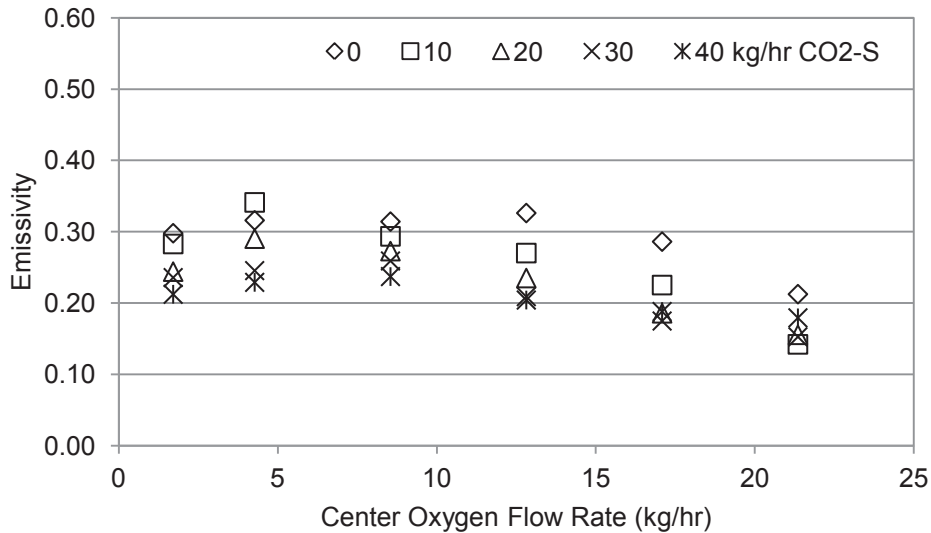

Figure 6-9. Emissivity as a function of center oxygen flow rate for each secondary CO_2 flow rate using the 15° swirl vane.

6.3   **40° Swirl Vane Temperature and Emissivity Results**

Table 6-3 is a matrix of representative flame images as a function of center oxygen and secondary CO_2 flow rates for the 40° swirl vane. For all conditions, the flame is attached as it exits the burner. Thus, the plot of lift-off length is not provided for this swirl setting. The flame luminosity, the inverse of the gain, is highest at 0 kg/hr CO_2-S and decreases with increasing CO_2-S. There does not appear to be a trend in flame luminosity with center oxygen flow rate. The flame appears to be narrower at high center oxygen flow rates (right column), favoring the right side of the viewing window at 0 and 20 kg/hr CO_2-S. Many of the flames show dark regions or clouds between the flame and the camera. These dark clouds were visible with the naked eye during operation and are thought to be composed of unburned, pulverized coal particles. These regions of unburned coal were periodic but steady at a given condition.

Table 6-3. Matrix of representative flame images for 40° swirl vane. Rows contain conditions at various secondary CO_2 flow rates; columns contain conditions at various center O_2 flow rates. Image gains are labeled above each image.

	1.7 kg/hr O_2-C	4.3 kg/hr O_2-C	8.5 kg/hr O_2-C	12.8 kg/hr O_2-C	17.1 kg/hr O_2-C	21.4 kg/hr O_2-C
0 kg/hr CO_2-S	GAIN=2	GAIN=2	GAIN=3.1	GAIN=2	GAIN=3.1	GAIN=2
20 kg/hr CO_2-S	GAIN=3.1	GAIN=3.1	GAIN=3.1	GAIN=3.1	GAIN=3.1	GAIN=2
40 kg/hr CO_2-S	GAIN=4.2	GAIN=4.2	GAIN=6.3	GAIN=5.2	GAIN=5.2	GAIN=5.2

For example, the flame at 0 CO_2-S and 21.4 kg/hr O_2-C is seen to be bright on the right side and dark on the left side of the window. The dark side contains unburned coal, presumably from an uneven distribution of coal in the primary annulus at the burner exit. This dark, left side was seen

73

in all ten representative images taken at this condition. A final observation about these flames is that they form a wrinkled, continuous flame sheet, particularly at low center oxygen and secondary CO_2 flow rates.

A possible explanation for the observed behavior of these flames is that the swirl produced by the 40° swirl vane in the primary fuel annulus created a condition where the coal particles were transported radially outward when they exited. The fuel tube was recessed 8.5 cm within the secondary tube. Due to the radial momentum of the coal, it was transported to the outer edges of the tube. Therefore, at the exit of the secondary tube, the coal and its volatiles were predominantly located on the outside of the oxidizer stream. Due to the coal location, the portion of the flame visible to the camera was more fuel rich. The sheet-like flames imaged for these conditions suggest that the turbulence is lower for this burner configuration. Perhaps, the more turbulent transport of oxidizer was on the inside of the fuel stream and not visible to the camera.

Figure 6-10 presents the spatially-averaged temperature results as a function of center oxygen flow rate for each secondary CO_2 flow rate using the 40° swirl vane. Generally, flames with higher secondary CO_2 flow rates are seen to have lower temperature. There are no strong trends with temperature produced by changes in center O_2 flow rates. The lack of a clear trend may be the result of partial or full flame blockage by unburned coal. Partial obscuration of the flame by coal will reduce the calculated flame temperature. Near total obscuration produces pixels with intensities low enough that they are excluded from the flame calculation and, thus, have no impact on the average temperature. The operating conditions produced repeatable locations where the flame was obscured. Therefore, a shift to a similar operating condition that

would normally cause a small change in flame temperature might cause a large shift in the location of unburned coal, and thus, a large difference in the inferred flame temperature.
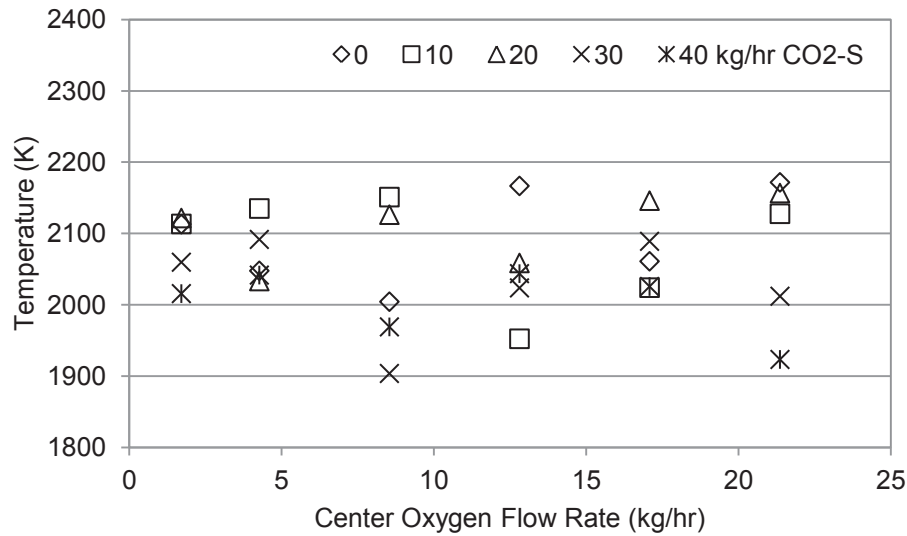
Figure 6-10. Temperature as a function of center oxygen flow rate for each secondary CO$_2$ flow rate using the 40° swirl vane.

Figure 6-11 presents the spatially-averaged emissivity results as a function of center oxygen flow rate for each secondary CO$_2$ flow rate using the 40° swirl vane. As with the temperatures, the emissivities obtained with the 40° swirl vane were scattered and did not produce strong trends with changes in secondary CO$_2$ or center oxygen flow rates. The average emissivities are higher for the 40° swirl vane than for the 0° and 15° swirl configurations. The observed obscuration of the flame by the pulverized coal may be partially responsible for the higher emissivities seen. Also, there is less mixing between the coal and oxidizer as can be seen in the images of the flame sheets. This results in increased soot formation, which also causes higher emissivities.
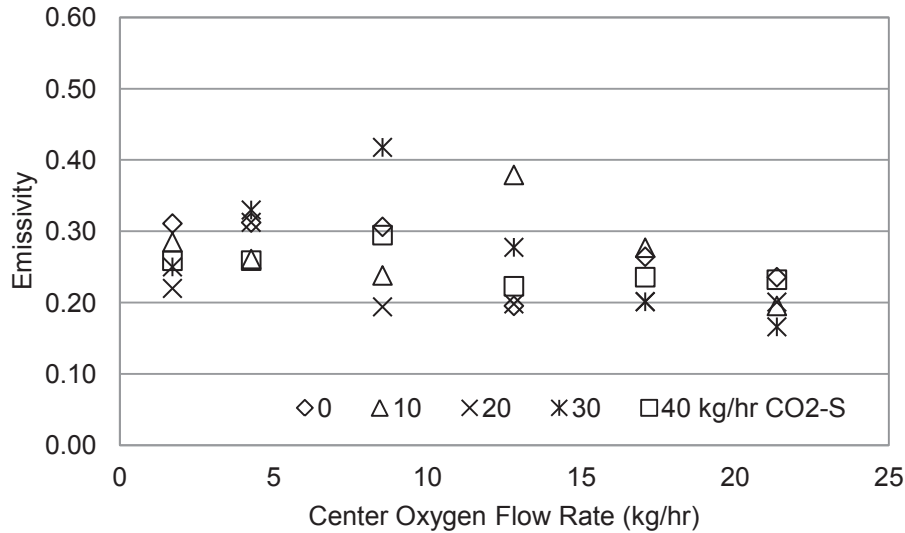
Figure 6-11. Emissivity as a function of center oxygen flow rate for each secondary CO$_2$ flow rate using the 40° swirl vane.

6.4 Axial Temperature and Emissivity Profile Results

Using the 2-D temperature and emissivity maps, the axial (distance from the burner in the axial direction) temperature and emissivity were calculated. A single axial temperature and emissivity were determined by averaging the temperature or emissivity within horizontal strips of 2.5 cm length. For example, a temperature marker at a distance of 5 cm gives the average temperature of all the pixels within the flame between 5 cm and 7.5 cm from the burner exit. A complete set of axial temperature plots are provided in the appendix. A selected set of data are shown here to provide a description of the temperature profiles. Table 6-4 shows the temperature and emissivity maps for two different flame conditions divided into the horizontal strips that are averaged to produce the profile graphs. The two conditions are provided to illustrate the difference in the demarcation between a flame with and without liftoff. The flame was defined to exist once 50% of the pixels in a row were contained within the flame boundary. Thus, for conditions with liftoff, the data does not begin immediately at the burner exit. The distance from

the burner exit was found using the ratio of the known width of the window to the number of

pixels in the imaged window width.

Table 6-4. Two conditions at different lift-off lengths presented with both temperature and emissivity maps to illustrate the subdivisions used to create the axial profile graphs.

No Lift-off		Lift-off	
Temperature	Emissivity	Temperature	Emissivity
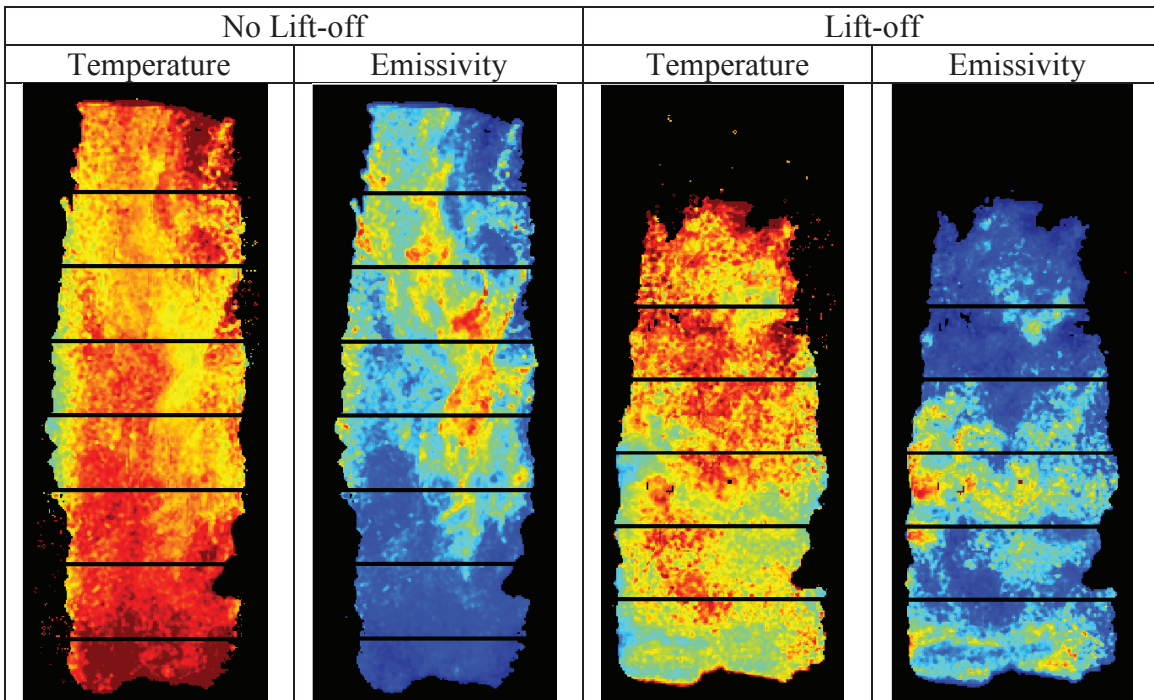
Matrices of graphs for temperature and emissivity axial profiles using no swirl vane and the 15 and 40° swirl vanes are shown in Table 6-5 through Table 6-10. Each row in the matrix contains conditions at a particular secondary CO_2 flow rate and each column contains conditions at a particular center oxygen flow rate. The profiles for three representative images are plotted in each profile graph to show the repeatability of that condition.

A general observation in almost all cases is that there are opposite trends in the axial temperature and emissivity profiles. When emissivity decreased, the temperature increased and vice versa. Interestingly, this trend is not observed in the magnitude of temperature and emissivity between different operating conditions. For example, consider the left column of Table 6-5. As CO_2-S increases, the magnitude of both the emissivity and temperature decrease.

One possible explanation for this observation is that the amount of diluent and the temperature of the mixture components prior to combustion in the flame determines the maximum adiabatic flame temperature. Thus, increasing the amount of cold CO_2 or recycled product gases that have lost heat to the walls decreases the adiabatic flame temperature. Thus, the decrease in temperature due to diluents is independent of flame emissivity. The inverse correlation between emissivity and temperature within a condition has at least two possible explanations. First, higher emissivity may be an indication of higher soot concentrations. Higher soot concentrations may cause higher rates of heat transfer and colder flames. A second possibility is that higher emissivity is indicated due to increased interference with cold coal particles. This interference also makes the temperature appear to be colder because of the absorption of light changing the ratio between the two colors in the measurement. As will be seen, the data are more consistent with the former argument suggesting that the emissivity is a measure of the amount of soot and that increased soot causes increased heat loss and lower flame temperatures. The key to understanding the temperature trends is therefore to understand the trends in soot concentration.

Soot is formed in fuel rich regions and is oxidized rapidly when passing through a flame. The radiation measured by the two-color method will be dominated by the soot in the flame front as it is being oxidized. This measured soot provides an indication of how much soot forms in the fuel rich boundary of the flame. Soot concentration will decrease when this mixture is leaner prior to ignition. Soot concentration will increase when the mixture is more fuel rich, or remains fuel rich without oxidizing, thereby allowing the soot concentration to increase prior to oxidation. Conditions described previously that produce lifted flames or enhance the mixing of oxidizer into the fuel stream will reduce soot. This decrease is seen by the decreased emissivity with increasing secondary CO_2 and center oxygen flow rates.

Using no swirl vane, the soot as a function of axial position tends to increase to a maximum and then decrease. The flame in most cases is lifted. This indicates that there is entrainment prior to ignition. It also indicates that the coal volatiles have not yet been heated and so have not yet released volatiles. Thus, the mixture is leaner near the burner and soot formation is low. As the volatile release increases relative to entrainment, the mixture becomes richer and soot formation increases. As the volatile release slows and entrainment continues, the mixture becomes leaner again and soot formation decreases. Most, if not all, of the data can be explained by the competing effects of the rate of oxidizer entrainment and the rate of volatile release at a given location. Since volatile release and entrainment rates were not measured, there is no definitive proof these rates correlate with the measured emissivity and therefore alternative explanations are possible.

Table 6-5. Axial (cm) temperature (K) profiles for no swirl vane. Rows contain conditions at various secondary CO_2 flow rates; columns contain conditions at various center O_2 flow rates.

Table 6-6. Axial (cm) emissivity profiles for no swirl vane. Rows contain conditions at various secondary CO$_2$ flow rates; columns contain conditions at various center O$_2$ flow rates.
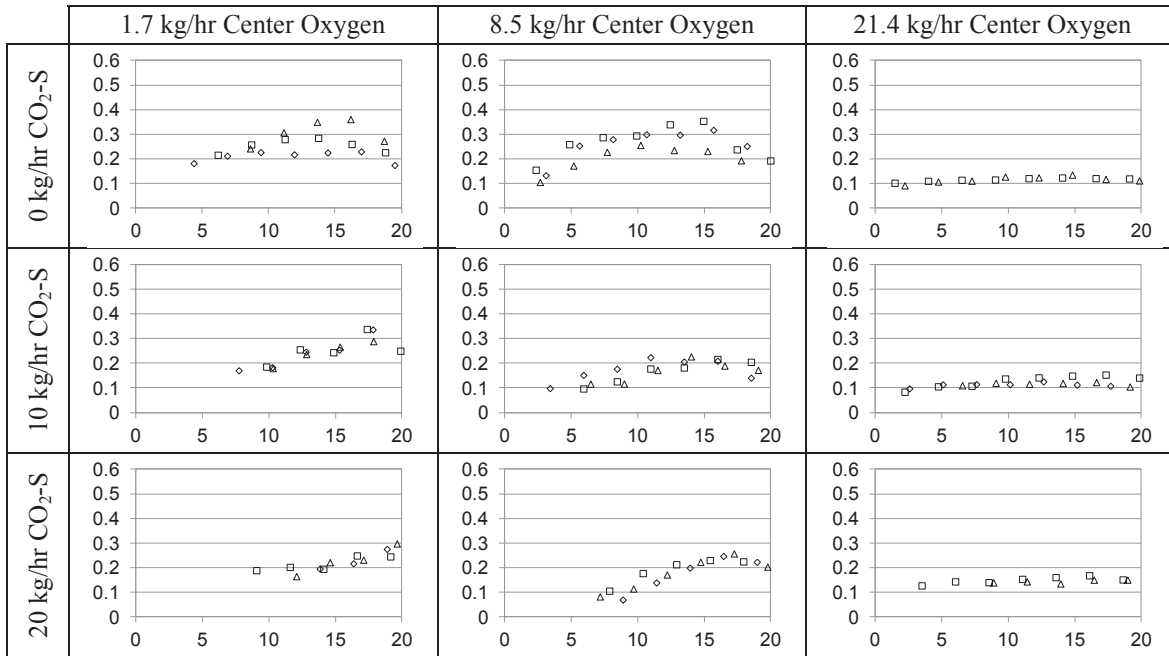
Table 6-7. Axial (cm) temperature (K) profiles for 15° swirl vane. Rows contain conditions at various secondary CO$_2$ flow rates; columns contain conditions at various center O$_2$ flow rates.
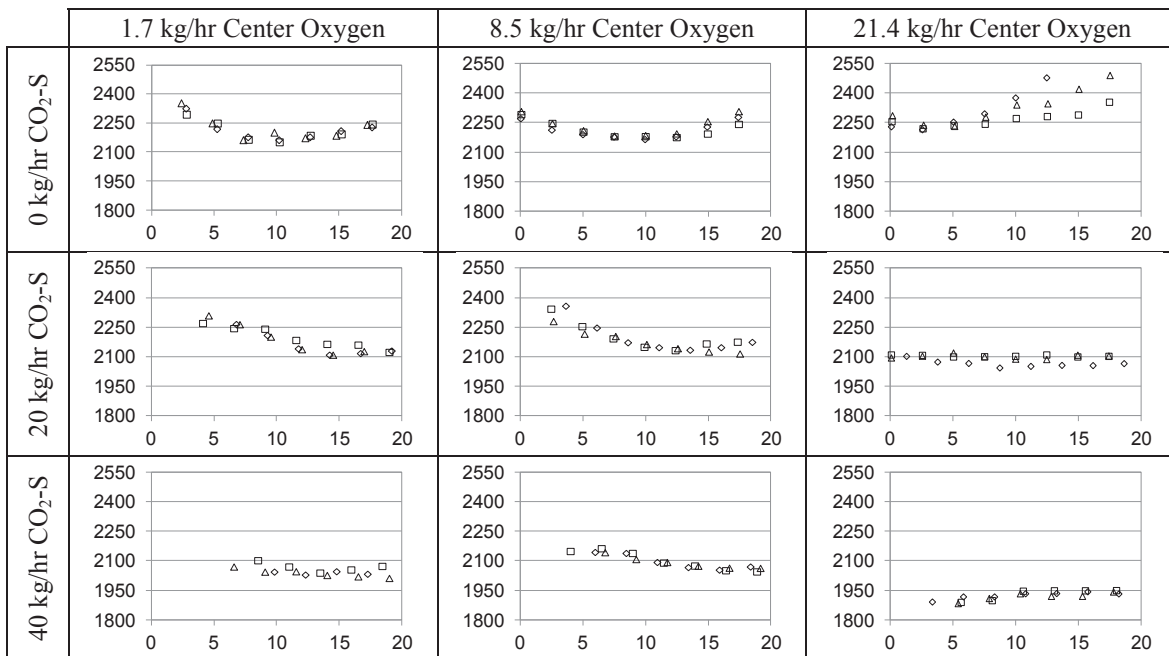
Table 6-8. Axial (cm) emissivity profiles for 15° swirl vane. Rows contain conditions at various secondary CO$_2$ flow rates; columns contain conditions at various center O$_2$ flow rates.
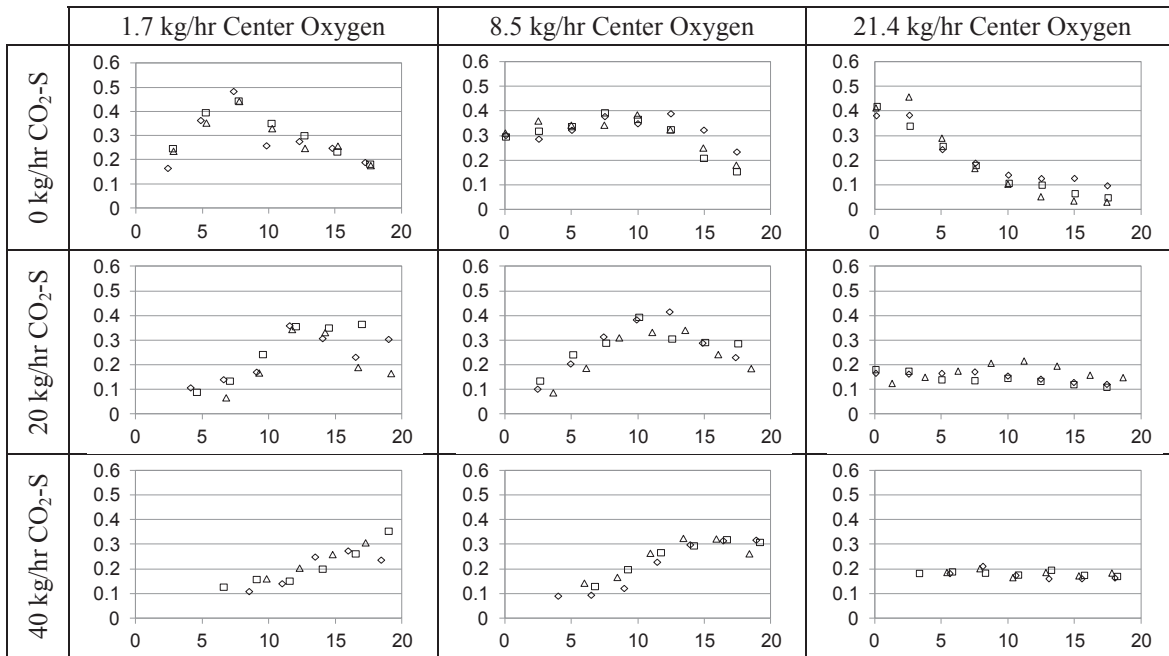
Table 6-9. Axial (cm) temperature (K) profiles for 40° swirl vane. Rows contain conditions at various secondary CO$_2$ flow rates; columns contain conditions at various center O$_2$ flow rates.
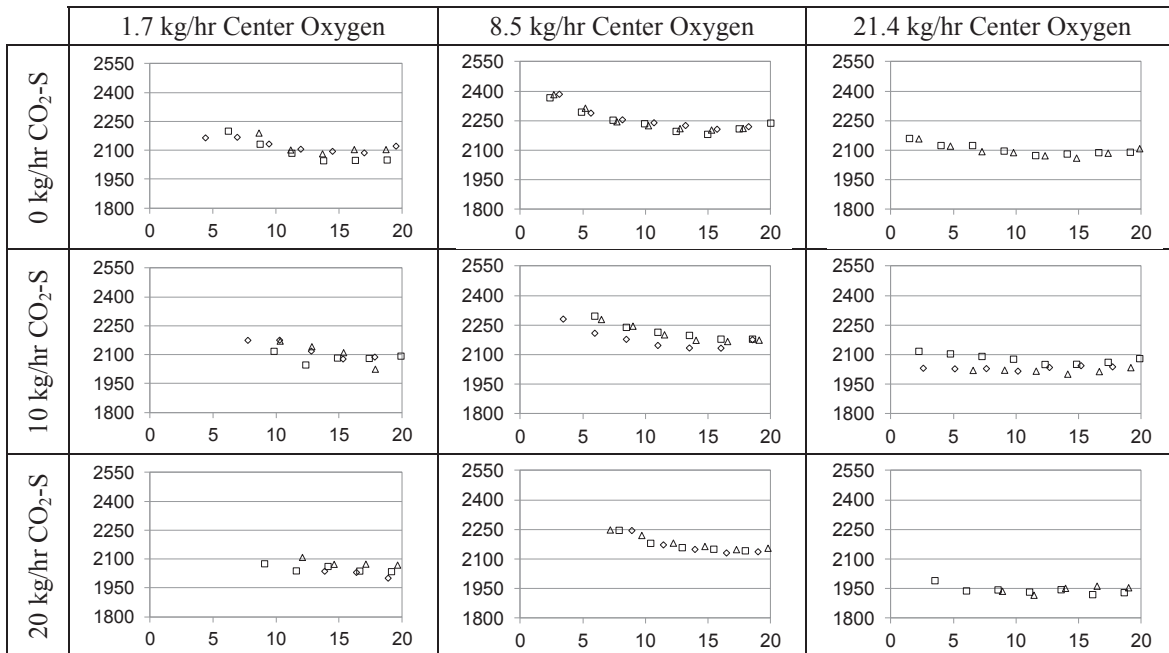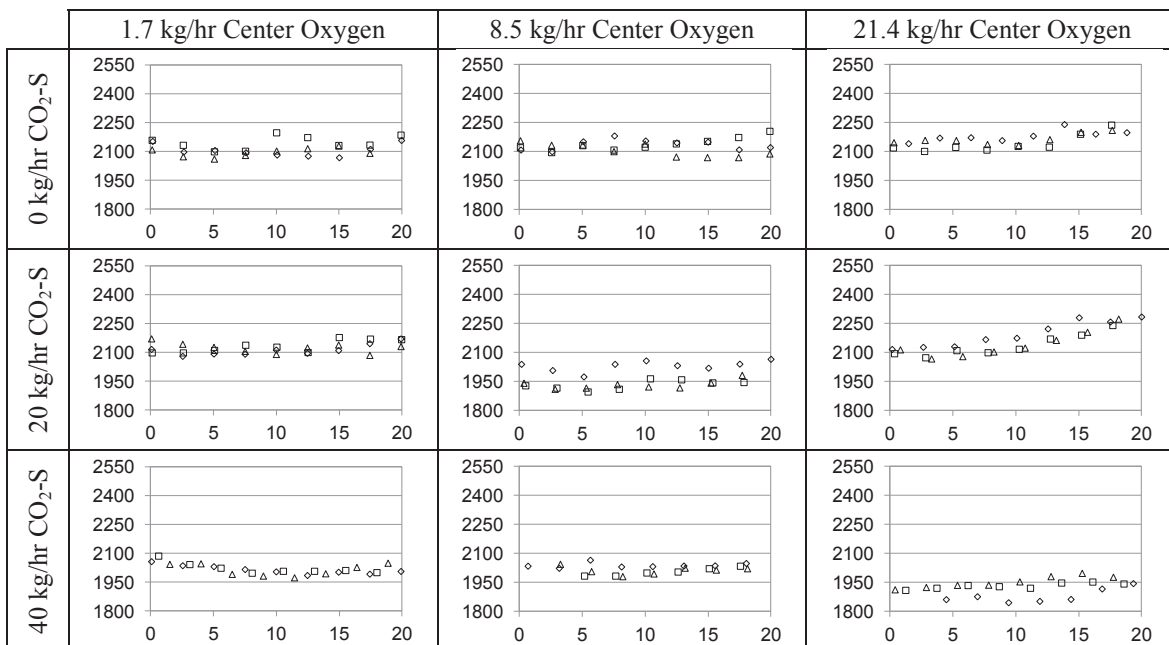
Table 6-10. Axial (cm) emissivity profiles for 40° swirl vane. Rows contain conditions at various secondary CO_2 flow rates; columns contain conditions at various center O_2 flow rates.
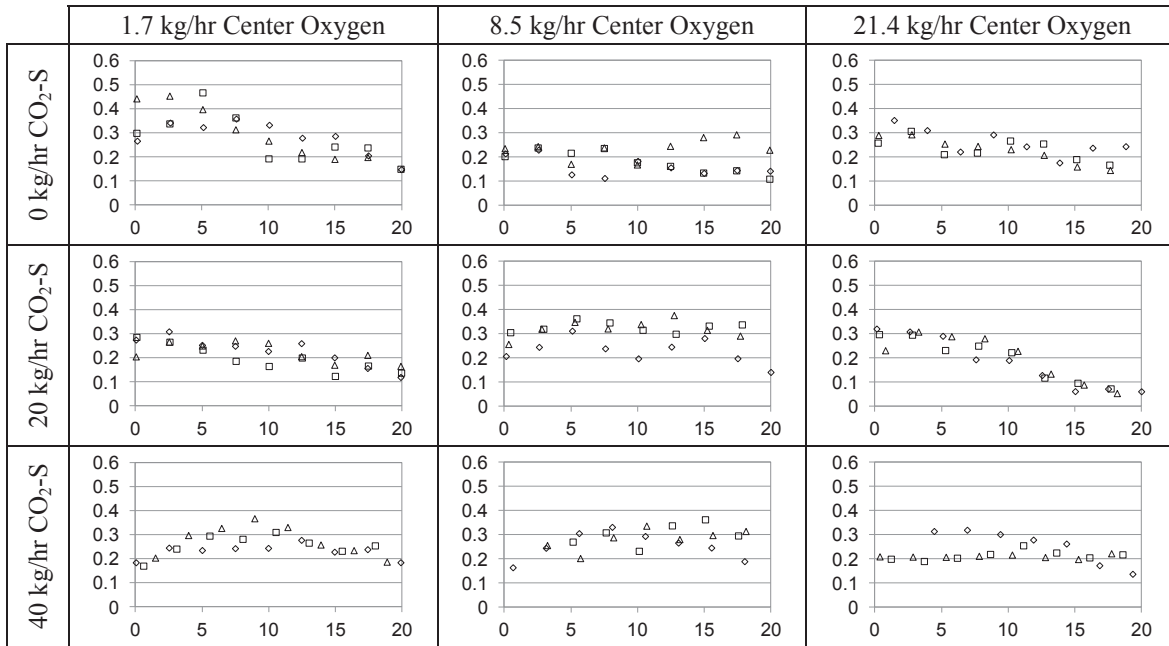
Once the emissivity is understood, the temperatures within an axial trend are seen to follow emissivity relatively well. Heat loss from soot is not the only variable impacting these temperatures and therefore, changes in the mixture fraction of the diluents and the flame temperature may also have an influence.

7 CONCLUSIONS AND FUTURE WORK

A digital color camera was calibrated and used to obtain images on a 150 kW$_{th}$, oxy-coal flame under a matrix of operating conditions which investigated the effects of oxygen addition location, the flow rate of CO_2 in the secondary, and the amount of swirl in the fuel stream. Two emissivity models, the Hottel and Broughton and the gray model, were investigated to determine which is most appropriate for use with two-color pyrometry in coal flames. The two models produced significantly different temperature (7%) and emissivity (24%) for the test case explored. It was concluded that the Hottel and Broughton emissivity model was the most appropriate in the near-burner region where the flame radiation is dominated by soot, but the gray assumption is more valid in regions dominated by char burnout. The Hottel and Broughton model was used for the remainder of the reported results. The use of a single, digital camera for two-color pyrometry is a useful tool that provides qualitative data regarding: flame symmetry, luminosity and turbulent mixing. Image processes provided a semi-quantitative lift-off length. Calibrated imaging also provides quantitative data, such as: average temperature and emissivity, two-dimensional temperature and emissivity maps, and profiles of temperature and emissivity as a function of axial distance in the flame. The two-color method has the advantage of being inexpensive, non-intrusive and appropriate for particle-laden flames. The system can image flames over a wide range of temperatures and has a relatively simple setup.

Using the images, the characteristics of an oxy-coal flame were analyzed. The flame temperature was found to decrease by: 1) The addition of CO_2 in the incoming oxidizer stream, 2) Increased entrainment of recirculated products (mainly CO_2 and H_2O) that had lost some heat to the walls and 3) High emissivity, or soot concentration, increasing radiative heat transfer from the flame. Entrainment of oxidizer and recirculated products decreased the local stoichiometry of the flame, which caused decreased emissivity (lower soot formation). The lift-off length could be decreased by: 1) Increasing the swirl angle, 2) Moving oxygen to the center primary tube and 3) Decreasing the secondary CO_2 flow rate. A combination of the flame images, temperature and emissivity were useful in interpreting flame behavior.

These results are anticipated to be of value to the energy industry for several reasons. A relatively simple and inexpensive diagnostic tool is presented that can measure two-dimensional temperature and emissivity in particle-laden flames. This diagnostic is particularly useful in oxy-combustion flames, which have the potential for temperatures greater than the capabilities of existing physical probes. The results presented here are the first to compare the Hottel and Broughton and gray emissivity models for use with two-color pyrometry in coal flames. These data have brought a new awareness to the importance of modeling the emissivity correctly. The results presented contribute to characterizing the effects of swirl angle, oxygen location and CO_2 dilution on the temperature, emissivity and lift-off length of an oxy-coal flame. These data have been combined with measured NO emissions and burnout for this burner in order to explain the burner performance in a concurrent study presented by Zeltner [3].

For future work, it is recommended that additional effort be devoted to finding the most appropriate emissivity model for use in pulverized-coal flames. While Hottel and Broughton is the most widely used emissivity model for soot, additional work should be done to confirm that

the Hottel and Broughton model is accurate for the soot produced by coal flames. Also, at some point in the flame, where the soot has burned out and the radiation is dominated by char and ash particles a different model must be used. Further work must be done to account for the varied emissivity at different locations in a coal flame.

To address both of these issues, it is suggested that a fiber optic cable and a spectrometer be used to examine the emissions from the flame over the entirety of the wavelength spectrum, not just in the visible band. This measurement would also provide a total emission measurement, or the heat flux from the flame, since the emissivity would be known at all wavelengths, not just in the visible region. Additionally, the pixel response from all three color bands produced by the RGB camera could be used to more accurately model the emissivity and analyze the temperature.

REFERENCES

[1]   U.S. Energy Information Administration, "Annual Energy Outlook 2011 with Projections to 2035," Yearly Report, Washington D.C., 2011.

[2]   M. J. Toftegaard, J. Brix, P. A. Jensen, P. Glarborg and A. D. Jensen, "Oxy-fuel combustion of solid fuels," *Progress in Energy and Combustion Science,* vol. 36, no. 5, pp. 581-625, 2010.

[3]   D. Zeltner, "Characterization of High Oxygen Participation Coal and Petroleum Coke Flames: NO, Burnout, Flame Temperature, and Emissivity Measurements," Brigham Young University, Provo, Expected June 2012.

[4]   W. M. Tolles, J. W. Nibler, J. R. McDonald and A. B. Harvey, "A Review of the Theory and Application of Coherent Anti-Stokes Raman Spectroscopy (CARS)," *Applied Spectroscopy,* pp. 253-271, 1977.

[5]   N. Ladommatos and H. Zhao, "A Guide to Measurement of Flame Temperature and Soot Concentration in Diesel Engines Using the Two-Colour Method Part 1: Principles.," *SAE Paper,* vol. 941956, 1994.

[6]   N. Ladommatos and H. Zhao, "A Guide to Measurement of Flame Temperature and Soot Concentration in Diesel Engines Using the Two-Colour Method Part 2: Implementation.," *SAE Paper,* vol. 941956, 1994.

[7]   S. di Stasio and P. Massoli, "Influence of the Soot Property Uncertainties in Temperature and Volume-Fraction Measurements by Two-Colour Pyrometry," *Measurement and Science Technology,* vol. 5, pp. 1453-1465, 1994.

[8]   H. Zhao and N. Ladommatos, "Optical Diagnostics for Soot and Temperature Measurement in Diesel Engines," *Progress in Energy and Combustion Science,* vol. 24, no. 3, pp. 221-255, 1998.

[9]   D. R. Tree and K. I. Svensson, "Soot Processes in Compression Ignition Engines," *Progress in Energy and Combustion Science Technology,* pp. 272-309, 2007.

[10]   D. W. Shaw and R. H. Essenhigh, "Temperature Fluctuations in Pulverized Coal (P.C.) Flames," *Combustion and Flame,* pp. 333-346, 1991.

[11]   G. Lu and Y. Yan, "Temperature Profiling of Pulverized Coal Flame Using Multicolor Pyrometric and Digital Imaging Techniques," *IEEE Transactions on Instrumentation and Measurement,* vol. 55, no. 4, pp. 1303-1308, 2006.

[12]   Y. Huang, Y. Yan and G. Riley, "Vision-based measurement of temperature distribution in a 500-kW model furnace using the two-colour method," *Measurement,* pp. 175-183, 2000.

[13]   C. Lou and H.-C. Zhou, "Deduction of the two-dimensional distribution of temperature in a cross section of a boiler furnace from images of flame radiation," *Combustion and Flame,* pp. 97-105, 2005.

[14]   W. Huajian, H. Zhifeng, W. Dundun, L. Zixue, S. Yipeng, F. Qingyan, L. Chun and Z. Huaichun, "Measurements on flame temperature and its 3D distribution in a 660 MWe arch-fired coal combustion furnace by visible image processing and verification by using an infrared pyrometer," *Measurement Science and Technology,* vol. 20, no. 11, pp. 114606-114618, 2009.

[15]   H. Lu, L.-T. Ip, A. J. Mackrory, L. Werrett, J. Scott, D. R. Tree and L. L. Baxter, "Particle Surface Temperature Measurements with Multicolor Band Pyrometry," *AIChE,* vol. 55, no. 1, pp. 243-255, 2008.

[16]   C. Lou, H.-C. Zhou, P.-F. Yu and Z.-W. Jiang, "Measurements of the flame emissivity and radiative properties of particulate medium in pulverized-coal-fired boiler furnaces by image processing of visible radiation," *Proceedings of the Combustion Institute,* vol. 31, no. 2, pp. 2771-2778, 2007.

[17]   K. I. Svensson, A. J. Mackrory, M. J. Richards and D. R. Tree, "Calibration of an RGB, CCD Camera and Interpretation of its Two-Color Images for KL and Temperature," *SAE Paper 2005-01-0648,* 2005.

[18]   L.-T. Ip, L. L. Baxter, A. J. Mackrory and D. R. Tree, "Surface Temperature and Time-Dependent Measurements of Black Liquor Droplet Combustion," *AIChE Journal,* vol. 54, no. 7, pp. 1926-1931, 2008.

[19]   Z. Jiang, Z. Luo and H. Zhou, "A Simple Measurement Method of Temperature and Emissivity of Coal-fired Flames from Visible Radiation Image and its Application in a CFB Boiler Furnace," *Fuel,* vol. 88, pp. 980-987, 2009.

[20] Y. Xue, C. Periasamy, T. Kang, R. Tsiava, F. Panier, B. Belasse, D. Zeltner, T. S. Draper and D. R. Tree, "Characteristics of a High Oxygen Participation Coal Burner," in *The 7th U.S. National Combustion Meeting*, Atlanta, Georgia, 2011.

[21] Y. Xue, C. Periasamy, T. Kang, R. Tsiava, F. Panier, B. Belasse, D. Zeltner, T. S. Draper and D. R. Tree, "Performance of Air Liquide's Oxy-Coal Burner with High Oxygen Participation Ratio," in *The 36th International Technical Conference on Clean Coal and Fuel Systems*, Clearwater, Florida, 2011.

[22] T. S. Draper, D. Zeltner, D. R. Tree, Y. Xue and R. Tsiava, "Two-Color Imaging of an Oxy-Coal Flame using an RGB, Digital Camera," in *The 36th International Technical Conference on Clean Coal and Fuel Systems*, Clearwater, Florida, 2011.

[23] K. I. Svensson, "Effects of Fuel Molecular Structure and Composition on Soot Formation in Direct-Injection Spray Flames," Brigham Young University, Provo, Utah, 2005.

[24] D. R. Tree and J. A. Peart, "Two-Color Transmittance Measurements in a Pulverized Coal Reactor," in *Proceedings of the Combustion Institute, Twenty-Eighth Symposium (International) on Combustion*, Edinburgh, Scotland, 2000.

[25] D. R. Tree, C. Stimpson and A. Fry, "Line of Sight Soot Measurements in Pulverized Coal Oxy Flame," in *The 35th International Technical Conference on Clean Coal and Fuel Systems*, Clearwater, Florida, 2010.

[26] T. H. Fletcher, J. Ma, J. Rigby, A. L. Brown and B. W. Webb, "Soot in Coal Combustion Systems," *Progress in Energy and Combustion Science,* vol. 23, pp. 283-301, 1997.

[27] A. L. Brown and T. H. Fletcher, "Modeling Soot Derived From Pulverized Coal," *Energy and Fuels,* vol. 12, pp. 745-757, 1998.

[28] M. Kerker, The Scattering of Light and Other Electromagnetic Radiation, New York: Academic Press, 1969.

[29] H. Hottel and F. Broughton, "Determination of True Temperature and Total Radiation from Luminous Gas Flames," *Industrial and Engineering Chemistry,* vol. 4, no. 2, pp. 166-175, 1932.

[30] F. Wang, X. J. Wang, Y. Z. Ma, J. H. Yan, Y. Chi, C. Y. Wei, M. J. Ni and K. F. Cen, "The research on the estimation for the NOx emissive concentration of the pulverized Coal Boiler by the Flame Image processing Technique," *Fuel,* vol. 81, pp. 2113-2120, 2001.

[31]   W. Li, C. Lou, Y. Sun and H. Zhou, "Estimation of Radiative Properties and Temperature Distributions in Coal-fired Boiler Furnaces by a Portable Image System," *Experimental Thermal and Fluid Science,* vol. 35, no. 2, pp. 416-421, 2011.

[32]   C. Yang, H. Zhou and Z. Huang, "Visualization of 3-D Temperature Distribution in a 300 MW, twin-furnace, Coal-fired Boiler," *Journal of China University of Mining & Technology,* vol. 18, pp. 0033-0037, 2008.

[33]   J. Smart, G. Lu, Y. Yan and G. Riley, "Characterisation of an Oxy-coal Flame Through Digital Imaging," *Combustion and Flame,* vol. 157, pp. 1132-1139, 2010.

[34]   G. Lu, Y. Yan, G. Riley and H. C. Bheemul, "Concurrent measurements of temperature and soot concentration of pulverised coal flames," *IEEE Transactions on Instrumentation and Measurement,* vol. 51, pp. 990-995, 2002.

[35]   C. R. Shaddix and A. Molina, "Particle imaging of ignition and devolatilization of pulverized coal during oxy-fuel combustion," *Proceedings of the Combustion Institute,* vol. 32, no. 2, pp. 2091-2098, 2009.

[36]   J. J. Murphy and C. R. Shaddix, "Influence of scattering and probe-volume heterogeneity on soot measurements using optical pyrometry," *Combustion and Flame,* vol. 143, no. 2005, pp. 1-10, 2004.

APPENDIX A.   AXIAL PROFILE RESULTS

This section presents the full set of axial profile temperature and emissivity results for the 0, 15 and 40° swirl vanes. The temperature and emissivity results for all the conditions taken at a particular swirl vane are presented as a matrix of graphs. The abscissas axis for each plot is the distance in centimeters from the burner exit and the ordinate axis is either the temperature in degrees Kelvin or the emissivity. Each row in the matrix contains conditions at a particular secondary CO_2 flow rate and each column contains conditions at a particular center oxygen flow rate.

A.1 No Swirl Vane Axial Profile Temperature and Emissivity Results

Table A-1. Axial (cm) temperature (K) profiles for no swirl vane. Rows contain conditions at various secondary CO₂ flow rates; columns contain conditions at various center O₂ flow rates.

91

Table A-2. Axial (cm) emissivity profiles for no swirl vane. Rows contain conditions at various secondary CO_2 flow rates; columns contain conditions at various center O_2 flow rates.

A.2 15° Swirl Vane Axial Profile Temperature and Emissivity Results

Table A-3. Axial (cm) temperature (K) profiles for 15° swirl vane. Rows contain conditions at various secondary CO₂ flow rates; columns contain conditions at various center O₂ flow rates.
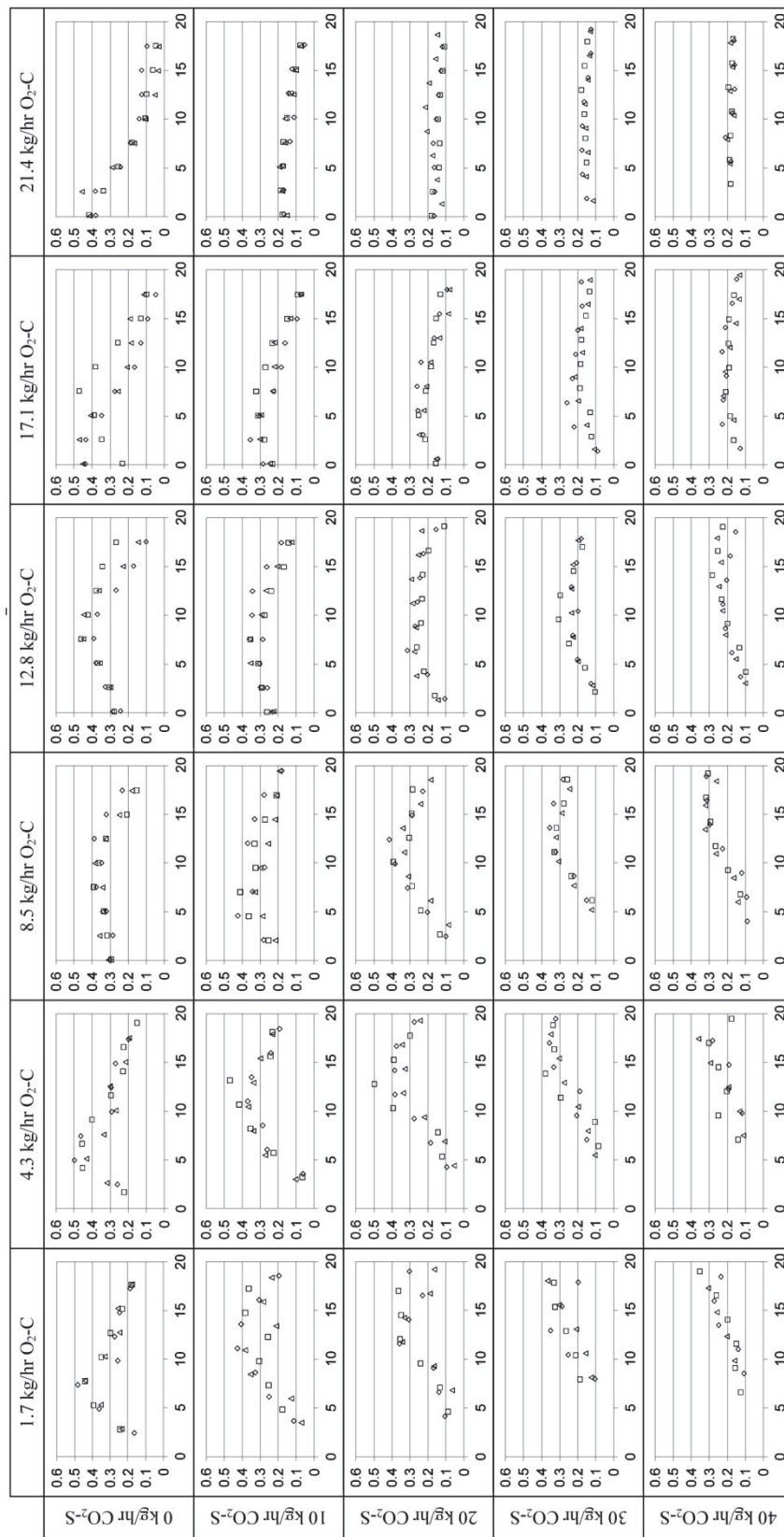
Table A-4. Axial (cm) emissivity profiles for 15° swirl vane. Rows contain conditions at various secondary CO_2 flow rates; columns contain conditions at various center O_2 flow rates.

A.3 40° Swirl Vane Axial Profile Temperature and Emissivity Results

Table A-5. Axial (cm) temperature (K) profiles for 40° swirl vane. Rows contain conditions at various secondary CO₂ flow rates; columns contain conditions at various center O₂ flow rates.
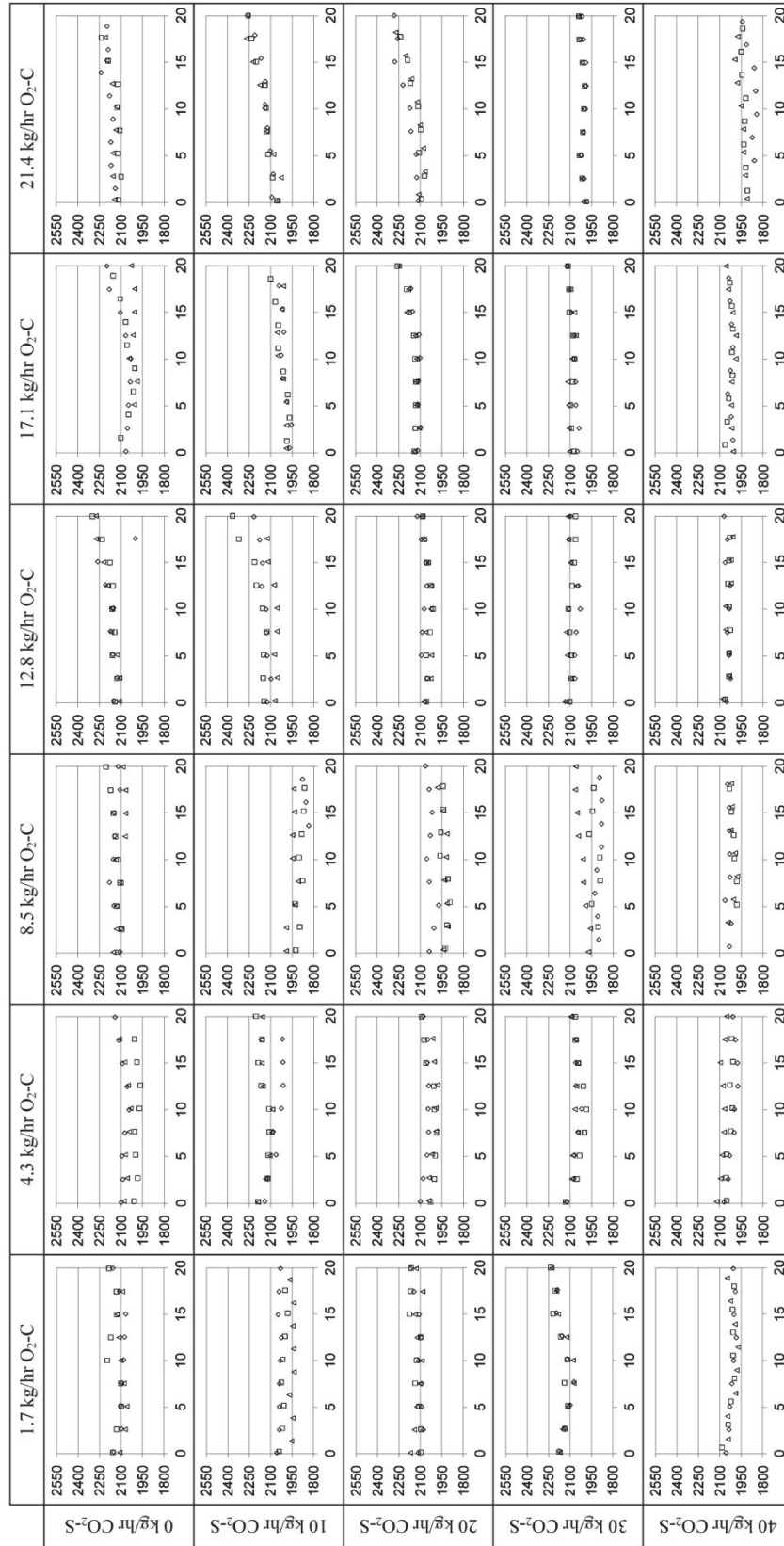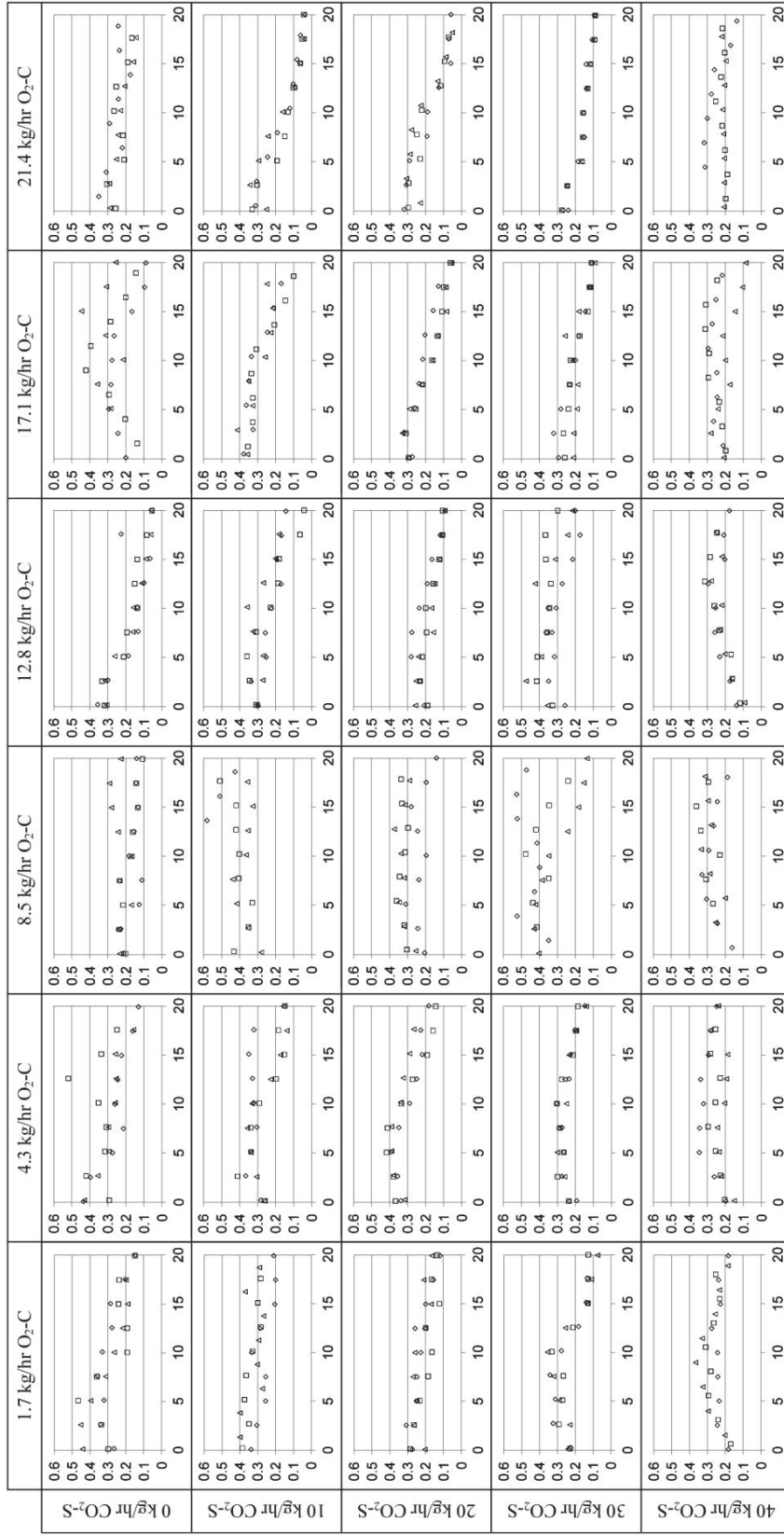
Table A-6. Axial (cm) emissivity profiles for 40° swirl vane. Rows contain conditions at various secondary CO_2 flow rates; columns contain conditions at various center O_2 flow rates.

APPENDIX B.   IMAGE PROCESSING DESCRIPTION

This section presents a description of the method used to process the images for the temperature and emissivity results. First, the pixel values from the image are pre-processed according to the calibration as found in Section 3.2. The flame boundary is found primarily through the use of a MATLAB-based edge finding algorithm. Finally, the MATLAB function "fsolve" is used to solve the non-linear governing equation for the temperature and KL values. The KL values are then used to find the visible band emissivity values.

B.1   Pre-processing Pixel Values

Each image is named in a standard format that contained the camera settings used to take the image. The code draws this information from the image name in order to process the data correctly. The name contains the neutral density filter used, the exposure time, the aperture setting, the date the image was taken and the image number. When the code is run, the user selects the image file to process and the MATLAB code imports the red, green and blue (RGB) pixie values for the image. The image is displayed and the user selects the area around the flame (Figure B-1), which crops the selected area from larger image. This prevents any reflection from the filters and windows in the optical setup from interfering with the edge finding algorithm.
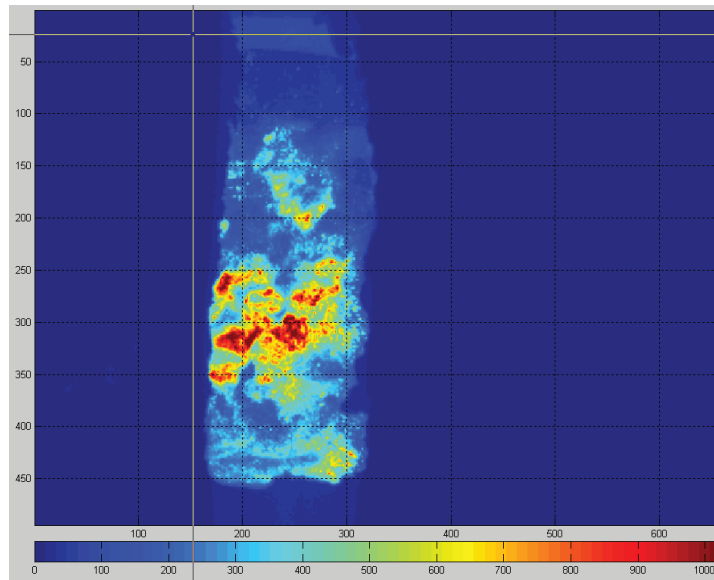
Figure B-1. User selects area around the flame from the original image to avoid interference from optical system reflections.

An error map is created to track pixels that are too dark or that are saturated. Pixels were defined to be too dark when they were below 30 and saturated when they were at the maximum value, 1023. The user is asked to select the desired binning and filtering sizes. Binning averages a square of pixel values to a single pixel. This reduces the resolution of the image but greatly increases the processing speed of the image. All data presented in this work did not use binning in order to have as high a resolution as possible; however, binning is quite useful for quickly examining results. Typical binning is over a 2x2 square of pixels. Median filtering utilizes the MATLAB function "medfilt2" and smoothes noise over a square of pixels while preserving the edges of the image. Typical filtering is over a 3x3 square of pixels. The pixels are adjusted for the initial energy correction, according to the calibration in Section 3.2. The pixels are also flat field corrected by dividing the pixel values by the flatfield correction matrix that correlates to the aperture setting used.

B.2　Flame Boundary Detection

The edge finding algorithm uses the MATLAB function "edge" and the Sobel method to find the flame boundary. The Sobel method finds the derivative between two neighboring pixels and marks an edge at points where the derivative is maximized. This method does well at finding the flame boundary, but sometimes requires user input to eliminate radiating surfaces that are not part of the flame, such as the burner block. Figure B-2 shows on the left a flame image with the edge found automatically by MATLAB, as marked by the red lines. It includes a section of the burner block at the top. The user must increase the threshold values for the edge algorithm until the red edging does not trace around any non-flame surfaces. This has been done in the right image in Figure B-2.
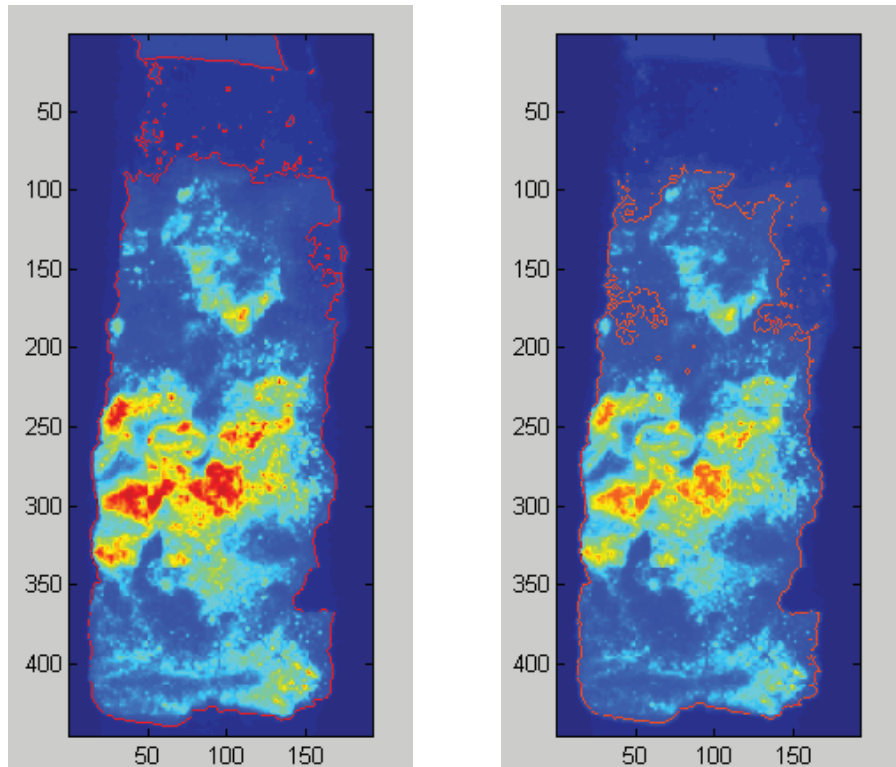

Figure B-2. Example of edge detection. Left: MATLAB output; Right: User adjusted MATLAB output.

B.3 Solving for Temperature and Emissivity Values

Once the flame boundary is defined, the MATLAB function "fsolve" is used to solve the governing equation (3-14) for the temperature and KL values. The "fsolve" function is used to solve systems of nonlinear equations with multiple variables of the form:

$$f(x, y) = 0. \tag{B-1}$$

Thus, the governing equation is rearranged to Equation (B-2) and the blue and red pixel values were used to solve for T and KL.

$$P_i - \int_{t_1}^{t_2} s_i A \int_{\lambda_1}^{\lambda_2} \left[1 - exp\left(\frac{-KL}{\lambda^\alpha} \right) \right] \left[\frac{C_1}{\lambda^5 \left(exp\left(\frac{C_2}{\lambda T} \right) - 1 \right)} \right] \beta_{\lambda,i} \varsigma_\lambda d\lambda \, dt = 0 \tag{B-2}$$

Pixels too dark or saturated are not used in the solver. If valid pixel values occur next to these invalid pixels, they are given the average temperature and KL of the valid neighbors. If the invalid pixels have no valid neighbors surrounding them, they are given a value of zero and the pixel location is marked on a solver map as not having solved. These pixels are not included when finding the average temperature and emissivity values. After the post-processing, the visible band emissivity was estimated from the KL values according to Equation (3-15) in Section 3.2.

The temperature and emissivity results are then analyzed. The temperature and emissivity maps are plotted, the average and maximum values are found, the lift-off length is calculated and the solver maps that mark which pixels did or did not solve are created. The temperature, emissivity and solver maps corresponding to the image in Figure B-1 and Figure B-2 are shown in Figure B-3. A small amount of pixels were saturated and did not solve. They are denoted by the dark red (Color 4 on the legend to the right) dots seen on the solver map. Other pixels were saturated but were near valid neighbors. These pixels are presented as the average of those

neighbors and are denoted by the orange dots (Color 3). All other pixels solved normally and are
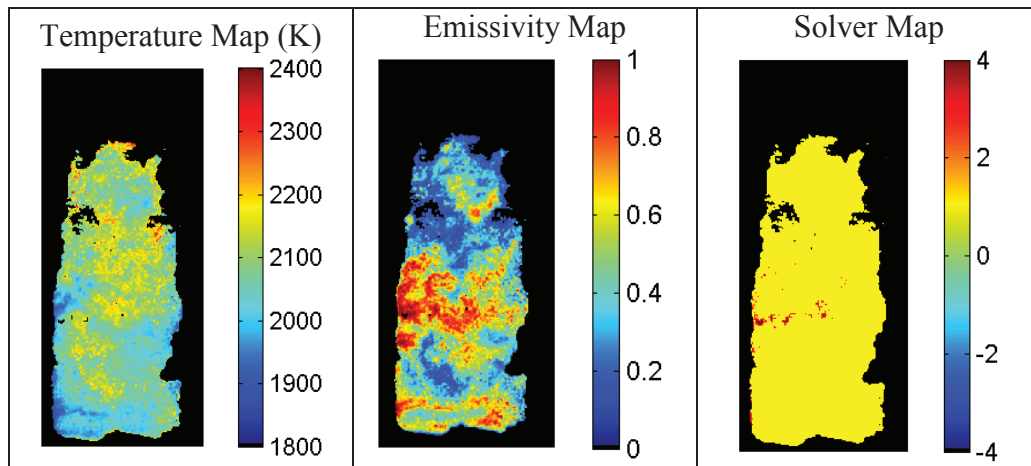
denoted by the yellow color (Color 1).

Figure B-3. Example of temperature, emissivity and solver maps.